Coordinated efforts of different actin filament populations are needed for optimal cell wound repair

Justin Hui[a], Mitsutoshi Nakamura[a], Julien Dubrulle[b], and Susan M. Parkhurst[a,*]
[a]Basic Sciences Division and [b]Cellular Imaging Shared Resource, Fred Hutchinson Cancer Center, Seattle, WA 98109

ABSTRACT **Cells are subjected to a barrage of daily insults that often lead to their cortices being ripped open and requiring immediate repair. An important component of the cell's repair response is the formation of an actomyosin ring at the wound periphery to mediate its closure. Here we show that inhibition of myosin or the linear actin nucleation factors Diaphanous and/or dishevelled associated activator of morphogenesis results in a disrupted contractile apparatus and delayed wound closure. We also show that the branched actin nucleators WASp and SCAR function nonredundantly as scaffolds to assemble and maintain this contractile actomyosin cable. Removing branched actin leads to the formation of smaller circular actin–myosin structures at the cell cortex and to slow wound closure. Removing linear and branched actin simultaneously results in failed wound closure. Surprisingly, removal of branched actin and myosin results in the formation of parallel linear F-actin filaments that undergo a chiral swirling movement to close the wound, uncovering a new mechanism of cell wound closure. Taken together, we demonstrate the roles of different actin substructures that are required for optimal actomyosin ring formation and the extraordinary resilience of the cell to undergo wound repair when it is unable to form different subsets of these substructures.**

Monitoring Editor
Laurent Blanchoin
CEA Grenoble

Received: May 5, 2022
Revised: Dec 2, 2022
Accepted: Dec 22, 2022

INTRODUCTION

All cells in the body undergo varying levels of physiological or environmental stress in response to normal daily events or as a result of diseases leading to fragile cells, such as muscular dystrophy or diabetes, that can cause damage to the cell cortex (plasma membrane and underlying cortical cytoskeleton;Galan and Bliska, 1996; Howard *et al.*, 2011; Cooper and McNeil, 2015). This damage initiates a cell's rapid repair programs to minimize further damage, prevent infection or cell death, and restore homeostasis (Velnar *et al.*, 2009; Sonnemann and Bement, 2011; Nakamura *et al.*, 2018). Cell wound repair is composed of three main events: 1) rapid plasma membrane resealing; 2) dynamic cytoskeletal reorganization for wound closure; and 3) membrane and cytoskeleton remodeling after wound closure to restore the cell cortex to its unwounded state. While there is a generally conserved framework among organisms, different molecular mechanisms have been described to achieve this repair (Bement *et al.*, 1999; Sonnemann and Bement, 2011; Nakamura *et al.*, 2018). In the *Drosophila* model, wound closure involves the formation, and then the constriction, of a Rho family GTPases-regulated actomyosin ring at the wound edge (Abreu-Blanco *et al.*, 2011a, 2011b, 2014; Nakamura *et al.*, 2018).

Rho family GTPases (Rho, Rac, Cdc42) are recruited to wounds in distinct spatiotemporal patterns (Abreu-Blanco *et al.*, 2014; Golding *et al.*, 2019). These proteins, through their downstream effector proteins, recruit actin to the wound, where it forms a dense actin ring bordering the wound edge (Abreu-Blanco *et al.*, 2011a, 2014; Nakamura *et al.*, 2017). The subsequent constriction of this actin ring

This article was published online ahead of print in MBoC in Press (http://www.molbiolcell.org/cgi/doi/10.1091/mbc.E22-05-0155) on January 4, 2023.

Competing interests: The authors declare no competing interests.

Author contributions: J.H., M.N., and S.M.P. contributed to the design of the experiments, performed experiments, and analyzed data. J.H. and J.D. performed morphometrics analyses. J.H. and S.M.P. wrote the manuscript with input from all authors.

*Address correspondence to: Susan M. Parkhurst (susanp@fredhutch.org).

Abbreviations used: AP, anterior–posterior; DAAM, dishevelled associated activator of morphogenesis; Dia, Diaphanous; DV, dorsal–ventral; GFP, green fluorescent protein; GLCM, gray level cooccurrence matrix; MLC, myosin light chain; NC, nuclear cycle; sfGFP, super folder green fluorescent protein; sGMCA, spaghetti squash driven, GFP, moesin-α-helical-coiled and actin binding site; sM3MCA, spaghetti squash driven, Maple3 fluorescent protein, moesin-α-helical-coiled and actin binding site; sqh, spaghetti squash; sStMCA, spaghetti squash driven, mScarlet fluorescent protein, moesin-α-helical-coiled and actin binding site; WAS, Wiskott–Aldrich syndrome.

© 2023 Hui *et al.* This article is distributed by The American Society for Cell Biology under license from the author(s). Two months after publication it is available to the public under an Attribution–Noncommercial-Share Alike 4.0 International Creative Commons License (http://creativecommons.org/licenses/by-nc-sa/4.0).

"ASCB®," "The American Society for Cell Biology®," and "Molecular Biology of the Cell®" are registered trademarks of The American Society for Cell Biology.

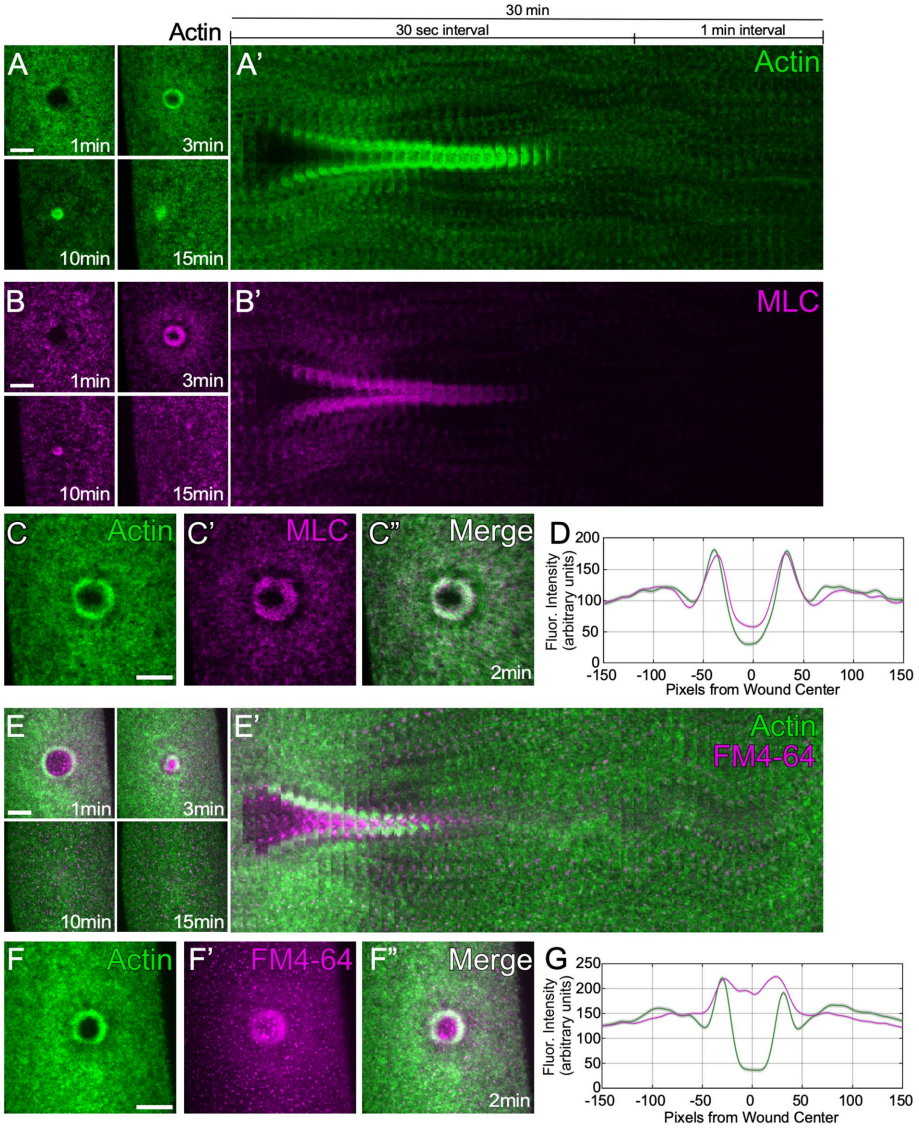

FIGURE 1: Cell wound repair in the Drosophila model requires a contractile actomyosin ring. (A, B) Confocal projection images of embryos expressing an actin reporter (sGMCA; A) and a fluorescent myosin transgene (sqh-StFP; B). (A′, B′) Kymographs across the wound area in A and B, respectively. (C–C″) Confocal projection images of embryos coexpressing the actin reporter (sGMCA; C, C″) and the fluorescent myosin transgene (sqh-StFP; C′, C″). (D) Fluoresence intensity (arbitrary units) profiles across the wound area in C″. (E, E′) Confocal projection images of embryos expressing an actin reporter (sGMCA) and FM4-64 dye injected into the perivitelline (extracellular) space. (F–F″) Confocal projection images of the actin reporter (F, -F″) and FM4-64 dye (F′, F″), (G) Fluoresence intensity (arbitrary units) profiles across the wound area in F″. Scale bars: 20 μm.

to pull the wound closed can be accomplished through different mechanisms. *Xenopus* oocytes can translocate the actin ring through myosin-independent actin treadmilling, the continuous assembly of actin at the inner edge and its disassembly at the outer edge of the actin ring (Burkel *et al.*, 2012). In the *Drosophila* cell wound model, the actin ring contracts in a myosin-dependent manner to close the wound (Abreu-Blanco *et al.*, 2011a,b; Nakamura *et al.*, 2018).

Downstream effectors of Rho family GTPases include both linear and branched actin nucleation factors. In general, linear actin nucleation factors function downstream of Rho, whereas branched actin nucleators function downstream of Rac and Cdc42 (Goley and Welch, 2006; Campellone and Welch, 2010; Courtemanche, 2018; Buracco *et al.*, 2019). Linear nucleation factors include Diaphanous-related formins (DRFs), which have been shown to affect actin ring formation in cell wound repair (Abreu-Blanco *et al.*, 2014; Hui *et al.*, 2022). Branched actin nucleation factors include the Wiskott–Aldrich syndrome (WAS) family proteins WASp, Scar/WAVE, and WASH (cf. Takenawa and Suetsugu, 2007). WAS family proteins polymerize branched actin through interaction with the Arp2/3 complex and often function to regulate dynamic actin organizations (Millard *et al.*, 2004; Takenawa and Suetsugu, 2007; Campellone and Welch, 2010; Burianek and Soderling, 2013; Massaad *et al.*, 2013; Alekhina *et al.*, 2017; Gautreau *et al.*, 2021; Kramer *et al.*, 2022).

Here we show that linear and branched actin nucleation factors exhibit distinct patterns of spatiotemporal recruitment to the wound edge, as well as distinct wound closure phenotypes, using the *Drosophila* cell wound repair model. Using superresolution microscopy we find that different actin architectures are formed around the wound edge when we independently knockdown the linear actin nucleation factors Diaphanous (Dia) and DAAM or the branched actin nucleation factors WASp or SCAR. We find that DAAM, WASp, and SCAR contribute to actin filament orientation as the actin filaments making up the actin ring exhibit a significant shift from random to anterior–posterior alignment. Additionally, in the removal of branched actin through Arp3 knockdown, excessively long linear actin filaments are observed, suggesting that branched actin serves as a scaffold for linear actin filaments. Last, we uncovered a new mechanism of wound closure when the cell was unable to form a proper contractile apparatus wherein parallel linear actin filaments would spiral inward to close the wound. Thus, our results highlight the complex interplay that takes place between linear and branched actin nucleation factors to facilitate proper actin ring architecture formation and dynamic closure for optimal cell wound repair.

RESULTS

Cell wound repair in the *Drosophila* model requires a contractile actomyosin ring to close the breach

To examine the role of actin nucleation factors in cell wound repair, wounds were generated by laser ablation on the lateral side of nuclear cycle 4–6 *Drosophila* embryos (see *Materials and Methods*). Wound closure in the *Drosophila* cell wound repair model requires the action of an actomyosin contractile ring (Abreu-Blanco *et al.*, 2011a). In control embryos, actin and myosin (myosin light chain [MLC]) accumulate in two adjacent regions: 1) a highly enriched ring at the wound edge, and 2) a less dense halo region encircling the actomyosin ring at the wound periphery (Figure 1, A–D;

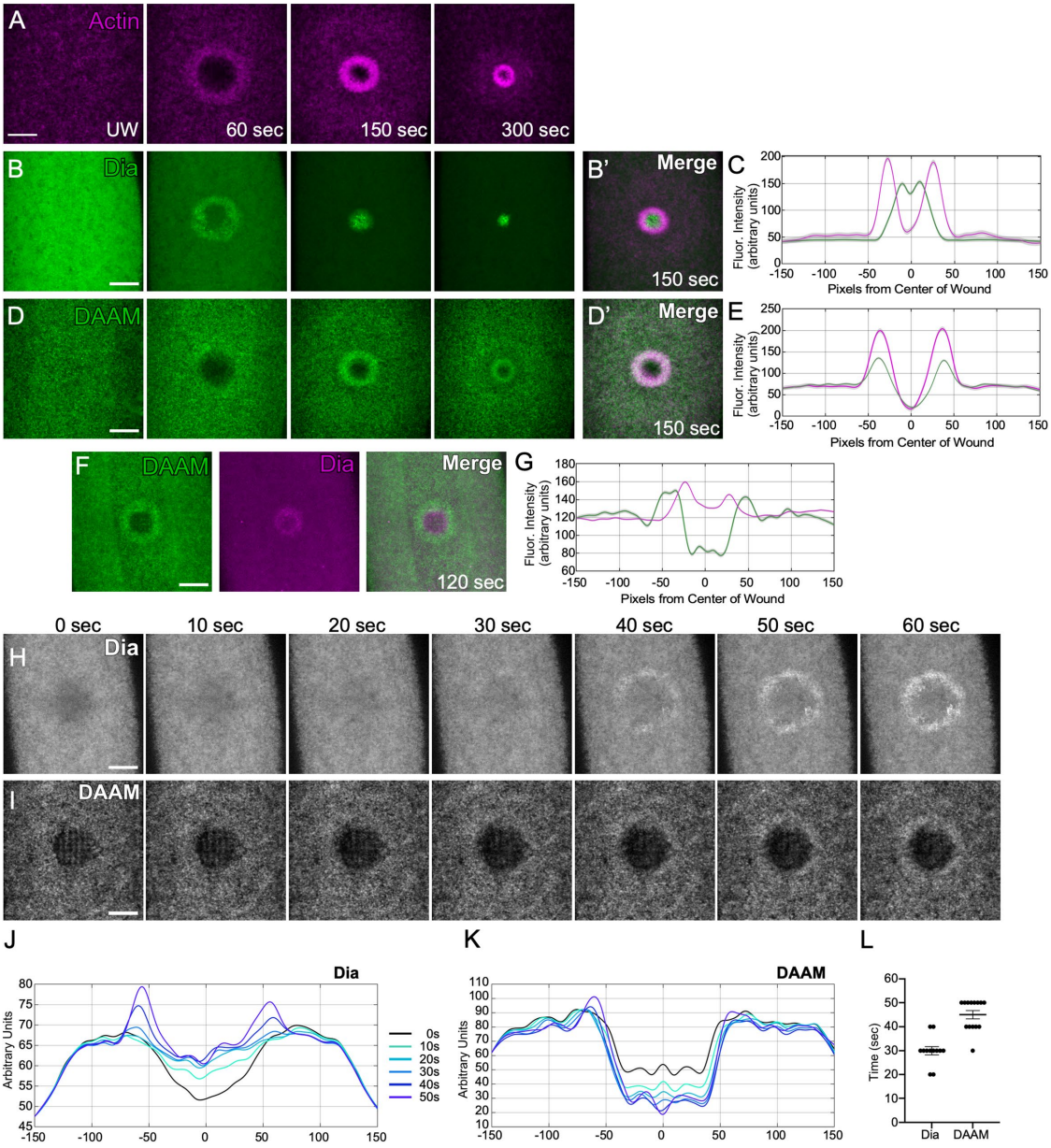

FIGURE 2: Dia and DAAM are recruited in distinct spatiotemporal patterns to the wound edge. (A–D′) Confocal projection images of embryos co-expressing an actin reporter (sGMCA; A) with GFP-Dia, B and B′, or DAAM-GFP, D and D′. (C, E) Fluorescence intensity (arbitrary units) profiles across the wound area in B′ and D′, respectively. (F) Confocal projection images of embryos co-expressing StFP-Dia and DAAM-GFP. (G) Fluorescence intensity (arbitrary units) profiles across the wound area in F. (H, I) Confocal projection images of GFP-Dia or DAAM-GFP acquired every 10 s. (J, K) Fluorescence intensity (arbitrary units) profiles across the wound area over time for the images shown in H and I. (L) Dotplot of initial Dia or DAAM recruitment to wounds. Scale bars: 20 μm.

Supplemental Table S1; Video 1). To visualize repair dynamics, a number of membrane or cytoskeleton fluorescent reporters or dyes are used in different cell wound repair systems (Hui *et al.*, 2022). As the cortical cytoskeleton is highly linked to the overlying plasma membrane and an actomyosin ring is formed at the periphery of wounds in the *Drosophila* model, actin reporters can be used interchangeably with membrane dyes to monitor the wound edge and repair dynamics in this model (Figure 1, E–G; Video 1).

The formins Dia and DAAM have distinct spatial and temporal recruitment patterns to cell wounds

Drosophila has seven *de novo* linear actin nucleation factors, including six formin homology proteins (Dia, DAAM, Cappuccino, Formin 3, Fhos, Formin-like) and Spire. We have shown previously that Dia is recruited to cell wounds (Abreu-Blanco *et al.*, 2014). To determine if other linear nucleation factors are recruited to cell wounds, we examined cell wound repair in embryos expressing GFP-tagged versions of each of these linear actin nucleation factor proteins (Figure 2, A–E; Supplemental Figure S1, A–H; Video 1). Upon laser injury, only Dia and DAAM are recruited to wounds (Figure 2, B–E; Supplemental Figure S1, A–H; Video 1). Interestingly, these exhibit distinct spatial recruitment patterns, with DAAM recruitment overlapping the actin ring, whereas Dia recruitment forms a ring that overlaps with the inner edge of the actin ring and extends to the inside of the wound (Figure 2, B′, C, D′–G; Video 1). Dia and DAAM also exhibit distinct temporal recruitment, with Dia present at 30 s postwounding and

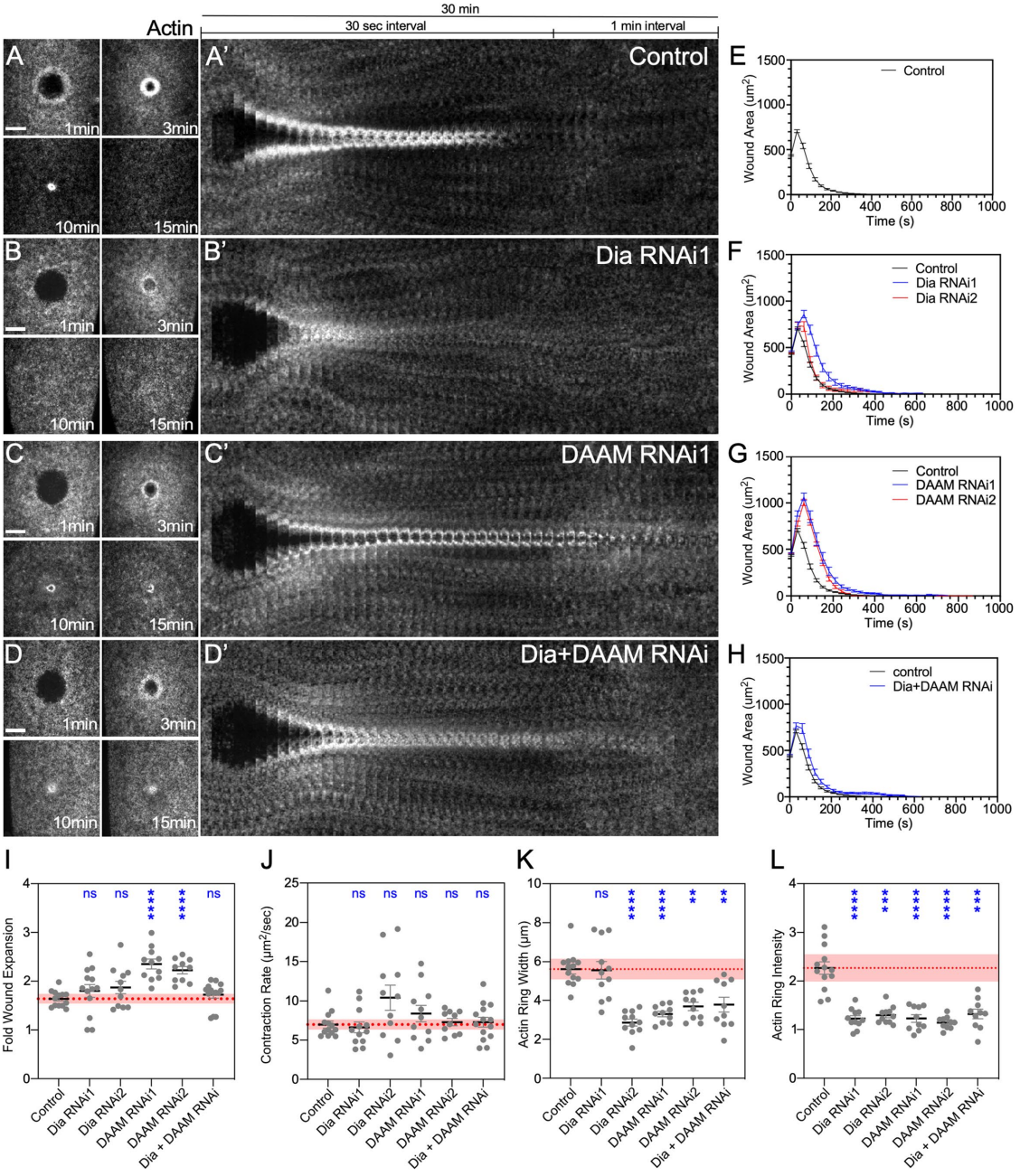

FIGURE 3: Linear actin is required for proper cellular wound repair and knockdown of Dia and DAAM exhibit non-redundant phenotypes. (A–D′) Actin dynamics (sGMCA) during cell wound repair: control (*vermilion* RNAi), A; Dia RNAi, B; DAAM RNAi, C; and Dia+DAAM RNAi, D. (A′–D′) XY Kymograph across the wound area depicted in A–D. (E–H) Quantification of wound area over time for control (*vermilion* RNAi, E; Dia RNAi, F; DAAM RNAi, G; and Dia+DAAM RNAi, H. (I–L) Quantification of fold wound expansion, I, wound contraction rate, J, actin ring width, K, and actin ring intensity, L. Black line and error bars represent mean ± SEM. Red dotted line and square represent mean ± 95% CI from control. Kruskal–Wallis test, I–L, with * $p < 0.05$, ** $p < 0.01$, *** $p < 0.001$, **** $p < 0.0001$, and ns not significant. Scale bars: 20 µm.

DAAM at 45 s postwounding (Figure 2, H–L). The distinct spatial and temporal recruitment of Dia and DAAM suggests that they have distinct functions during the cell wound repair process.

Knockdown of Dia or DAAM results in distinct defects in wound healing dynamics

Following the differences observed in the spatiotemporal recruitment patterns of Dia and DAAM, we expected these factors to exhibit distinct effects on cell wound repair. To investigate this, we expressed an actin reporter (sGMCA; Kiehart *et al.*, 2000) in Dia and/or DAAM knockdown backgrounds (Figure 3; Supplemental Figure S1, I–L′; Video 2). Knockdown embryos were generated by expressing RNAi constructs in the female germline using the GAL4-UAS system (Brand and Perrimon, 1993; Rorth, 1998), using two independent RNAi lines each for Dia and DAAM (Figure 3, A–F; Supplemental Figure S1, I–L′; Supplemental Figure S2). Dia knockdown resulted in lower actin accumulation around the wound and premature actomyosin ring disassembly, while retaining a normal wound closure

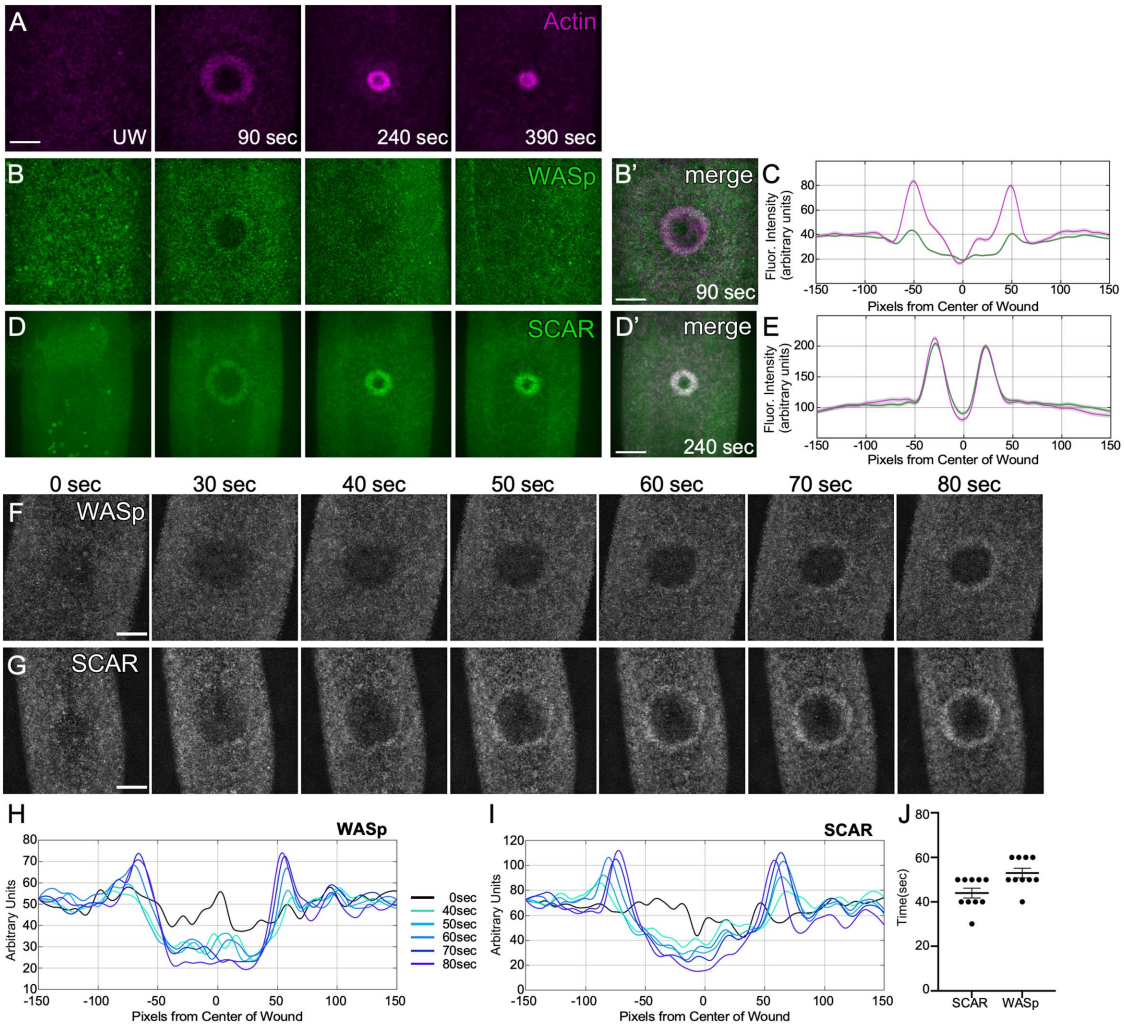

FIGURE 4: WASp and SCAR are recruited in distinct temporal patterns to the wound edge. (A–D′) Confocal projection images of embryos coexpressing an actin reporter (sGMCA), A, with GFP-WASp, B and B′, or GFP-SCAR, D and D′. (C–E) Fluorescence intensity (arbitrary units) profiles across the wound area in B′–D′, respectively. (F, G) Confocal projection images of GFP-WASp or GFP-SCAR acquired every 10 s. (H, I) Fluorescence intensity (arbitrary units) profiles across the wound area over time for the images shown in F and G. (J) Dot plot of initial WASp or SCAR recruitment to wounds. Scale bars: 20 μm.

rate and actin ring width (Figure 3, A, B′, E, F, I–L; Supplemental Figure S1, K and K′; Supplemental Table S2; Video 2). Interestingly, while DAAM knockdown also resulted in lower actin accumulation around the wound, it exhibited a failure to disassemble the actomyosin ring. In addition, DAAM knockdowns exhibited wound overexpansion and decreased actin ring width (Figure 3, C,C′, G, I–L; Supplemental Figure S1, L and L′; Supplemental Table S2; Video 2).

Because Dia and DAAM exhibit nonoverlapping cell wound repair phenotypes, we examined wound repair in Dia+DAAM double-knockdown embryos, where linear actin nucleation contribution should be minimal or nonexistent with respect to cell wound repair. The Dia+DAAM double knockdown resembles the DAAM knockdown—reduced actin ring width/intensity and failure to disassemble the actomyosin ring—with the exception of not exhibiting a wound overexpansion phenotype (Figure 3, D, D′, H–L; Supplemental Table S2; Video 2). These results demonstrate that Dia and DAAM are needed for optimal cell wound repair, that they exhibit both overlapping and nonredundant roles during the repair process, and that cell wound repair can occur, albeit more slowly, in the absence of linear actin nucleation factors.

WASp and SCAR have distinct temporal recruitment patterns to cell wounds

Because wound closure still occurs when linear actin nucleation factors are knocked down, we examined the role of branched actin nucleation factors in cell wound repair. To determine if and how WAS family members are recruited to cell wounds, we expressed GFP-tagged WAS proteins, along with an actin reporter (sStMCA) (Figure 4A; Video 3; Nakamura *et al.*, 2020). Upon laser injury, all WAS family members are recruited to wounds, although in distinct temporal recruitment patterns (Figure 4, B–G; Supplemental Figure S3, A and B; Video 3). WASp is recruited to the wound with a peak accumulation at 90 s, where it transiently colocalizes with the actin ring before dispersing by 240 s post injury (Figure 4, B and C; Video 3). SCAR recruitment overlaps with the actin ring and shows a peak accumulation at 240 s (Figure 4, D and E; Video 3). Wash shows only slight recruitment to the wound edge (Supplemental Figure S3, A and B). While Wash knockdowns disrupt cell wound repair (Supplemental Figure S3, C–I), Wash appears to play only a minor role in the repair process and we do not include it in the remaining analyses.

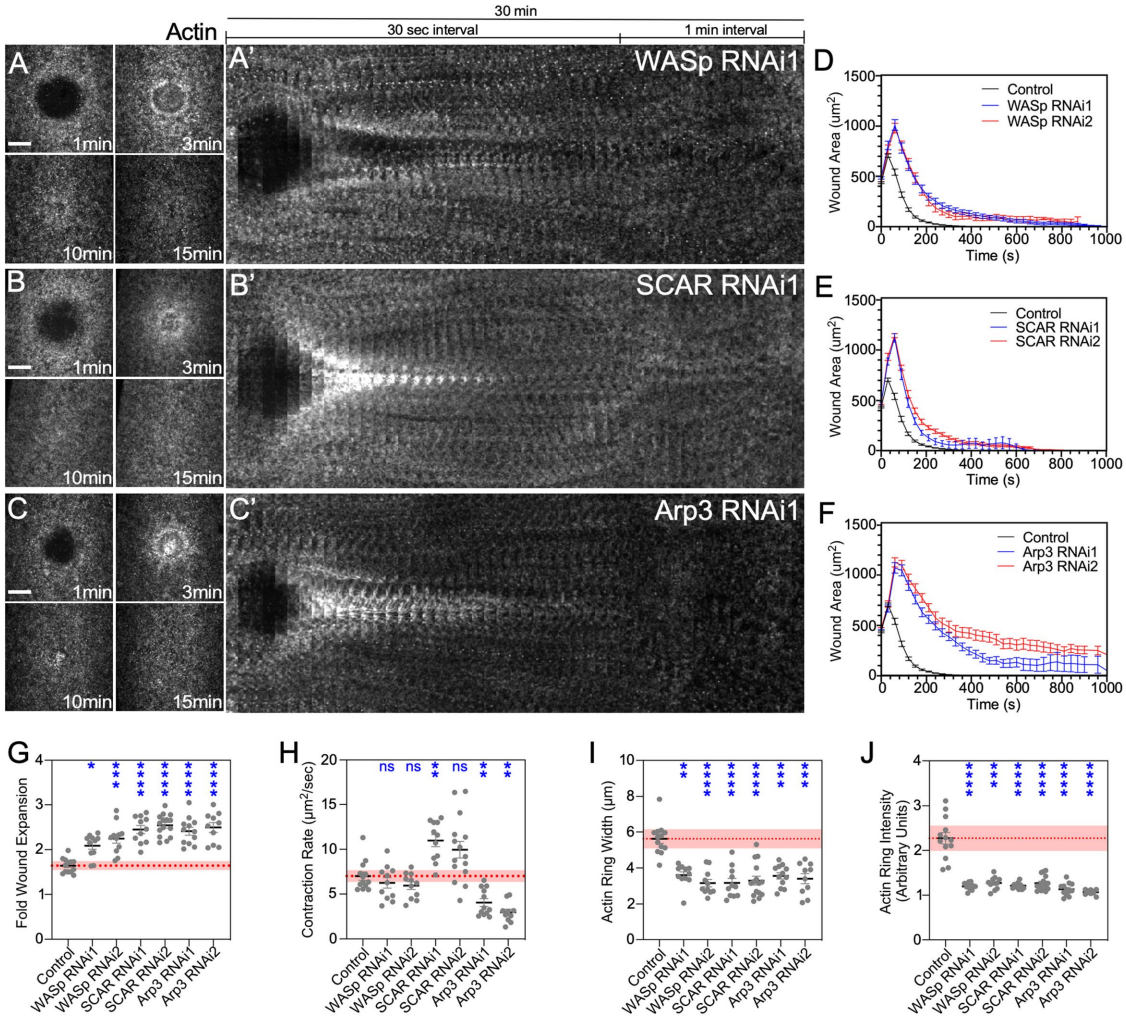

FIGURE 5: Branched actin is required for proper cellular wound repair, and knockdown of WASp and SCAR exhibit nonredundant phenotypes. (A–C) Actin dynamics (sGMCA) during cell wound repair: WASp RNAi, A, SCAR RNAi, B, and Arp3 RNAi, C. (A'–C') XY kymograph across the wound area depicted in A–C. (D–F) Quantification of wound area over time. (G–J) Quantification of fold wound expansion, G, wound contraction rate, H, actin ring width, I, and actin ring intensity, J. Black line and error bars represent mean ± SEM. Red dotted line and square represent mean ± 95% CI from control. Kruskal–Wallis test (G–J) with * $p < 0.05$, ** $p < 0.01$, *** $p < 0.001$, **** $p < 0.0001$, and ns not significant. Scale bar: 20 µm.

In addition to different peak recruitment times, the initial recruitment of WASp and SCAR to wounds is different. SCAR recruitment to wounds is first observed at 45 s postwounding, whereas the initial recruitment of WASp is only detected at 55 s postwounding (Figure 4, F–J). Thus, WASp and SCAR are recruited to the wound periphery in different dynamic temporal patterns suggesting that they have distinct functions during cell wound repair.

Knockdown of WASp or SCAR results in distinct defects in wound healing dynamics

To examine the effects of branched nucleation factors on cell wound repair, we expressed an actin reporter in WASp and SCAR knockdown backgrounds, using two independent RNAi lines for each (Figure 5, A–E, G–J; Supplemental Figure S1, I–L; Supplemental Figure S2; Video 4). Distinct cell wound repair phenotypes were observed in embryos lacking each of these WAS family proteins. WASp knockdown resulted in minimal actin accumulation around the wound with a smaller actin ring width, lower actin ring intensity, and wound overexpansion as compared with controls (Figure 5, A, A', D, G–J; Supplemental Figure S4, A and A'; Supplemental Table S2; Video 4). Interestingly, knockdown of WASp did not show a significant difference in contraction rate compared with controls (Figure 5H; Supplemental Table S2). Wounds generated in WASp knockdown fail to close completely within the 30-min time lapse and exhibited loose actin accumulation at the center of the wound that is not observed in control embryos (Figure 5, A, A', D, G–J; Supplemental Figure S4, A and A'; Video 4).

Similarly to WASp, SCAR knockdown also resulted in significantly smaller actin ring widths, lower actin ring intensity, and severe wound overexpansion as compared with control wounds (Figure 5, B, B', E, G–J; Supplemental Figure S4, B and B'; Supplemental Table S2; Video 4). However, in contrast to WASp, SCAR knockdown increased the wound contraction rate (Figure 5, B, B', E, G–J; Supplemental Figure S4, B and B'; Supplemental Table S2; Video 4). These results demonstrate that, similarly to Dia and DAAM, WASp and SCAR are required for proper cell wound repair and that they exhibit both overlapping and nonredundant roles during the repair process.

Scar/WAVE has recently been shown to induce actin protrusions in mammalian and *Dictyostelium* cells in an Arp2/3-independent manner (Buracco *et al.*, 2022). To test whether SCAR has Arp2/3-independent function during cell wound repair, we examined actin dynamics during wound repair in the SCAR+Arp3 double knockdown background. Wound repair in the double knockdowns is similar to that in Arp3 knockdown alone (Supplemental Figure S4, D–I), suggesting that SCAR is working in an Arp2/3-dependent manner in our system.

Knockdown of Arp3 results in impaired branched actin nucleation

WAS proteins activate the Arp2/3 complex by facilitating the presentation of a G-actin monomer that works with Arp2 and Arp3 subunits to begin branched actin nucleation. We expected that knockdown of Arp3 would mimic the combined loss of WASp and SCAR (as well as any potential contribution by Wash), thereby eliminating the majority of branched actin nucleation. As expected, Arp3 knockdown results in profound effects on cell wound repair: significantly less actin accumulation at the wound edge, smaller actin ring width, and premature dissociation of actin ring structures from the surrounding actin cortex (Figure 5, C, C′, F–J; Supplemental Figure S1, C and C′; Supplemental Table S2; Video 4). Arp3 knockdown embryos also exhibit greater wound overexpansion and a significantly slower contraction rate (Figure 5, G and H; Supplemental Table S2). Thus, Arp3 knockdown exhibits a combination of cell wound repair phenotypes observed in WASp and SCAR knockdowns individually. Taken together, WAS proteins and their cofactor Arp2/3 play nonredundant and important roles in optimal cell wound repair, likely by influencing the spatiotemporal patterns of branched actin assemblies.

Linear and branched actin nucleation factors coordinate actin ring filament architecture

Because Dia/DAAM, WAS proteins, and Arp2/3 influence the formation of linear or branched actin filaments and their assembly into different higher order architectures, we examined actin dynamics following injury using superresolution microscopy in Dia/DAAM, WAS, and Arp3 knockdowns. We captured the spatiotemporal differences in actin filament organization at the wound edge at both 50% and 70% wound closure (Figure 6). With the exception of Arp3, RNAi knockdown of these actin regulators does not significantly alter actin expression levels or organization before wounding (Supplemental Figure S2; Supplemental Table S3). Consistent with previous measurements of actin ring intensity (Figure 3L), the actin ring in control embryos has a greater density of actin recruitment (Figure 6, A and A′″).

To visualize the different actin organizations within the actomyosin ring, single *z*-slice images of wounds at 70% closure were deconvolved and used for further analyses (see *Materials and Methods*; Figure 6, A″–G″). To quantify the bulk actin architectural differences, we performed texture analysis using Haralick features (Variance, Correlation, Uniformity, and Homogeneity; see *Materials and Methods*) that together reflect actin mesh organization and density (cf. Nakamura *et al.*, 2020). Plotting these Haralick features on a radar chart, we observe a consistent pattern of altered actin ring architecture at wounds in Dia/DAAM versus WAS knockdown embryos that both differ significantly from the architecture observed in control wounds (Figure 6, H–Q; Supplemental Table S3). In particular, the actin organization of all knockdown wounds exhibited a significant decrease in variance and a significant increase in homogeneity and correlation compared with controls (Figure 6, O–Q; Supplemental Table S3). Similarly, DAAM, WASp, SCAR, and Arp3 knockdowns exhibited a significant increase in the uniformity of actin organization, whereas Dia exhibited a marginal increase (Figure 6Q; Supplemental Table S3).

Reduction of branched actin by Arp3 knockdown exhibited the most pronounced phenotype, with the formation of striking circular actin structures in the unwounded state (Figure 6G), limited actin recruitment around the wound, and long linear actin filaments at the center and around the wound (Figure 6, G′–G′″). In contrast, knockdown of Dia, DAAM, WASp, or SCAR alone did not exhibit the circular actin structures (Figure 6, B–F) or the pronounced linear actin filaments (Figure 6, B″–F″, B′″–F′″) observed in Arp3 knockdown. These results indicate that knockdown of either branched or linear actin causes severe, yet distinctive, disruptions to the actin filament architecture of the contractile actomyosin ring at the wound edge.

DAAM, WASp, and SCAR are required for actin filament orientation at the wound edge

To further differentiate the roles of actin nucleators, we conducted actin filament orientation analyses by measuring the magnitude and direction of intensity gradients of actin filaments/bundles at the wound edge and expressing them as the ratio of filament orientations between 80°–90° (anterior–posterior alignment; AP) and 0°–10° (dorsal–ventral alignment; DV)—orientation bias; see *Materials and Methods* (Figure 6, R–X). Control actin rings exhibited fairly uniform distribution of actin filaments (Figure 6R) and a random orientation bias (Figure 6R). Consistent with their colocalization with the actin ring, DAAM, WASp, Arp3, and to a lesser extent SCAR, knockdowns exhibited a shift toward AP actin filament orientation (Figure 6, T, V–X). Actin filaments in Dia and Dia+DAAM knockdowns did not exhibit statistically significant actin filament orientation shifts (Figure 6, S–U), consistent with the majority of Dia localizing to the inside of the actin ring. Our results indicate critical roles for DAAM, WASp, SCAR, and Arp3 in maintaining proper actin filament orientation at the wound edge. The lack of a clear orientation bias in Dia knockdown highlights its distinct function in cellular wound repair from DAAM or WAS proteins.

Circular actin structures associate with myosin, Dia, and DAAM

Upon removal of branched actin (Arp3 knockdown), the unwounded cell cortex exhibits a striking accumulation of circular actin filament structures (actin circles) 0.6–1.3 μm in diameter (Figure 7, A–C). Although some of these actin circles are present in the cortices of control embryos, embryos lacking branched actin have significantly more actin circles per region analyzed (control: 0.2 ± 0.09, $n = 20$; Arp3 RNAi: 11.8 ± 1.1, $n = 20$, $p < 0.0001$; Figure 7, A–C). To examine the potential role of these altered actin structures, we expressed mScarlet-tagged myosin light chain (MLC; sqh-StFP), GFP-Dia, or DAAM-GFP, along with a fluorescent actin reporter, in an Arp3 RNAi background. We find that MLC associates with the majority of actin circles (67%; Figure 7, D and E, F–I′), and does so in various patterns: accumulating in proximity to the actin circle (29%), filling the inside of the actin circle (13%), or only partially filling the actin circle (25%; Figure 7, F′–I′). In contrast, Dia and DAAM were only observed to associate with 39% and 46% of the actin circles, respectively (Figure 7, J–Q′). The association of MLC with the actin circles suggests an intriguing possibility that myosin bends and curls the untethered linear actin filaments into circular structures. Indeed, we observe linear actin filaments bending into circles in Arp3 knockdowns (Figure 7R). Further, we find that MLC, Dia, and to a lesser extent DAAM associate with the long linear actin filaments that accumulate at the center of the wound (Figure 7, D, E, J, K, N, and O), suggesting that the presence of Dia may prevent myosin from circularizing these actin filaments.

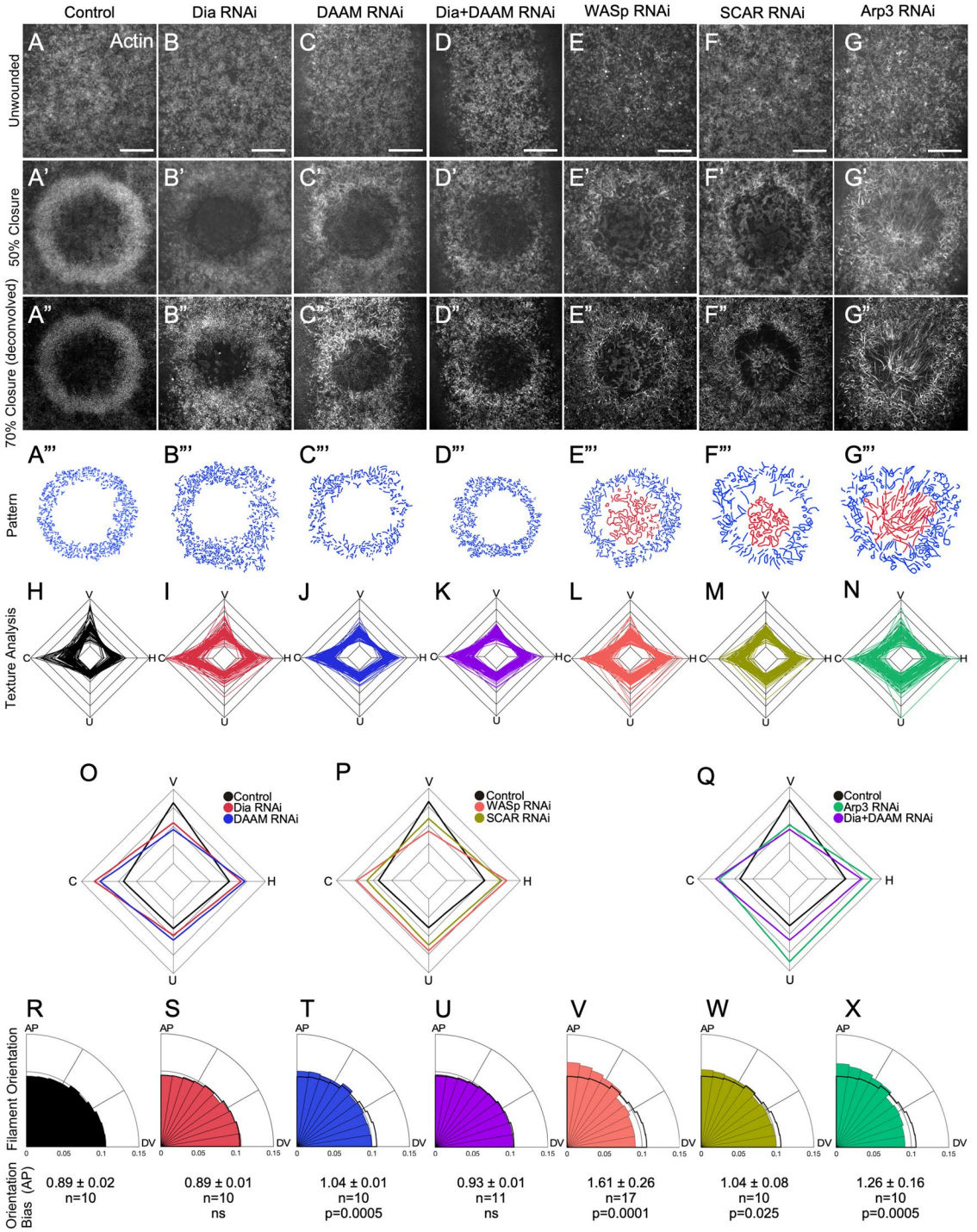

FIGURE 6: Individual knockdowns of actin nucleators exhibit different actin architectures at the wound edge. (A–G″) Super-resolution confocal images from embryos expressing an actin reporter (sGMCA) in control (*vermilion* RNAi), A–A″; Dia RNAi, B–B″; DAAM RNAi, C–C″; Dia+DAAM RNAi, D–D″; WASp RNAi, E–E″; SCAR RNAi, F–F″; and Arp3 RNAi, G–G″. (A–G) Unwounded actin cortex: control, A, Dia RNAi, B, DAAM RNAi, C, Dia+DAAM RNAi, D, WASp RNAi, E, SCAR RNAi, F, and Arp3 RNAi, G. (A′–G″) Single-slice images of the injury site at 50%, A′–G′, and 70%, A″–G″, of max wound area of embryos shown in A–G, respectively. (A‴–G‴) Hand-traced drawings showing actin filament organization in A″–G″, respectively (blue: actin ring; red: actin internal to wound edge). (H–N) Radar charts depicting calculated Haralick features (variance, V, homogeneity, H, uniformity, U, and correlation, C) in actin rings from control (*vermilion* RNAi), H; Dia RNAi, I; DAAM RNAi, J; Dia+DAAM RNAi, K; WASp RNAi, L; SCAR RNAi, M; and Arp3 RNAi, N. (O) Radar chart of average Haralick features comparing control, Dia RNAi, and DAAM RNAi. (P) Radar chart of average Haralick features comparing control, WASp RNAi, and SCAR RNAi. (Q) Radar chart of average Haralick features comparing control, Dia+DAAM RNAi, and Arp3 RNAi. (R–X) Radial histograms showing the distribution of actin filament orientations ranging from anterior–posterior (AP) bias to dorsal–ventral (DV) bias of control, R; Dia RNAi, S; DAAM RNAi, T; Dia+DAAM RNAi, U; WASp RNAi, V; SCAR RNAi, W; and Arp3 RNAi, X. Kruskal–Wallis test, R–X; all *p*-values indicated. Scale bar: 10 μm.

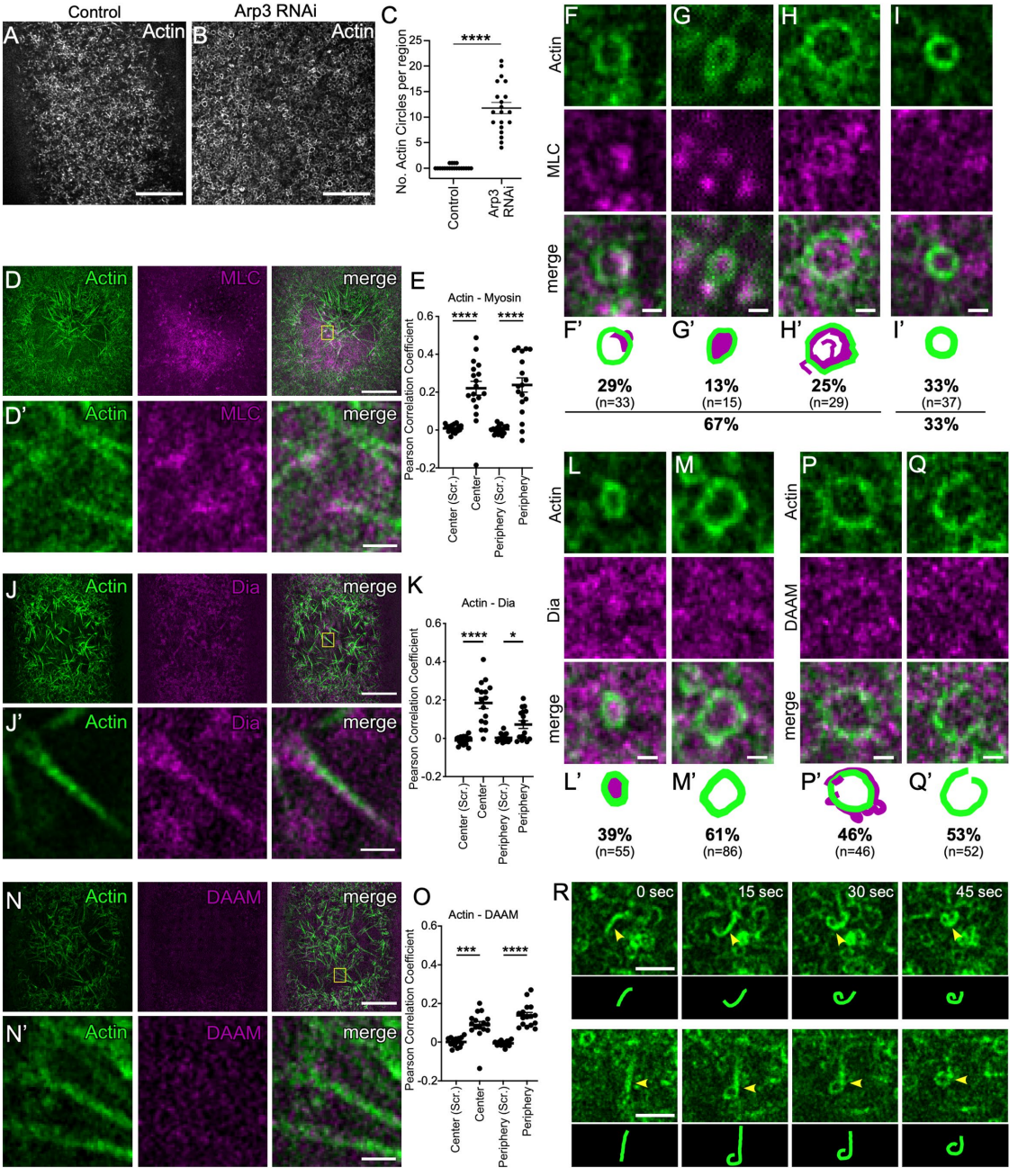

FIGURE 7: New circular actin structures form in the absence of branched actin. (A,B) Deconvolved single-slice confocal images of the unwounded cortices of embryos expressing an actin reporter (sGMCA) in control (*vermilion* RNAi), A and Arp3 RNAi, B. (C) Quantification of the number of actin circles per region (380 μm^2) in A and B. (D, D′) Deconvolved single-slice confocal images of Arp3 RNAi embryos coexpressing an actin reporter (sGMCA) and a fluorescent myosin light-chain (MLC) reporter (sqh-StFP) at 5 min postwounding. Higher-magnification view of yellow highlighed region, D′. (E) Pearson correlation coefficients of actin and myosin at either the wound center or wound periphery. Spatially scrambled (Scr) myosin images were used as controls. (F–I′) Higher-magnification view and quantifcation of actin circle and myosin associations observed. Drawings depicting actin circle and myosin association patterns shown in F–I, respectively, F′–I′. (J, J′) Deconvolved single-slice confocal images of Arp3 RNAi embryos coexpressing actin (sStMCA) and GFP-Dia reporters. Higher-magnification view of yellow highlighted region, J′. (K) Pearson correlation coefficients of actin and Dia at either the wound center or wound periphery. Spatially scrambled (Scr) Dia images were used as control. (L–M′) Higher-magnification view and quantification of actin circle and Dia association. Drawings depict actin circle and Dia association, L′, M′. (N, N′) Deconvolved single-slice confocal images of Arp3 RNAi embryos coexpressing actin (sStMCA) and DAAM-GFP reporters. Higher-magnification view of yellow highlighted region, N′. (O) Pearson correlation coefficients of actin and DAAM at either the wound center or the wound periphery. Spatially scrambled (Scr) DAAM images were used as controls. (P–Q′) Higher-magnification view and quantification of actin circle and DAAM association. Drawings depicting actin circle and DAAM association, P′, Q′. (R) Time-series images showing actin filaments rolling up to form actin circles. Welch's *t* test, C, E, K, O: * $p < 0.05$, ** $p < 0.01$, *** $p < 0.001$, **** $p < 0.0001$, ns not significant. Scale bars: 0.5 μm, F–I, L–Q; 1 μm, D′, J′, N′; 2 μm, R; 10 μm, A, B, D, J, N.

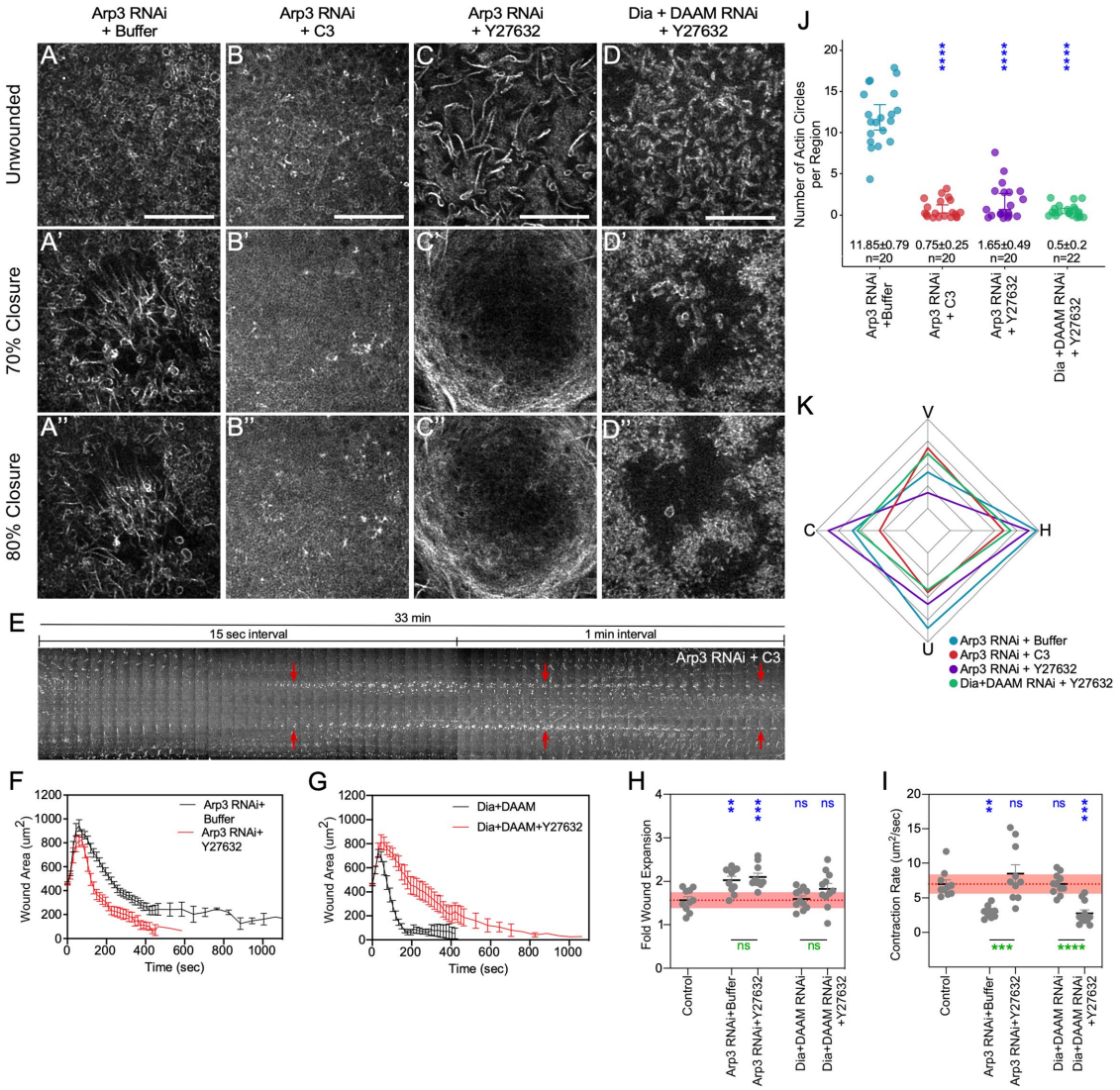

FIGURE 8: Both branched and linear actin are vital to wound repair. (A–C″) Superresolution confocal images of embryos coexpressing an actin reporter (sGMCA) and Arp3 RNAi that have been treated with buffer only (control), A–A″; C3 exoenzyme, B–B″; or Y27632, C–C″. (D–D″) Superresolution confocal images of embryos expressing an actin reporter (sGMCA) in Dia RNAi + DAAM RNAi and treated with Y27632. (A′–D″) Deconvolved single slice images of the injury site at 70%, A′–D′, and 80%, A″–D″, of max wound area of embryos shown in A–D, respectively. (E) XY Kymograph of embryo expressing an actin reporter (sGMCA), Arp3 RNAi, and treated with C3 exoenzyme showing that the wound edge (red arrow) does not close over time. (F–G) Quantification of wound area over time for Arp3 RNAi+Buffer and Arp3 RNAi+Y27632, F, and Dia+DAAM RNAi and Dia+DAAM+Y27632, G. (H, I) Quantification of fold wound expansion, H and wound contraction rate, I. (J) Quantification of the number of actin circles in a 300 × 300–pixel area of the unwounded cortex. (K) Radar chart of average Haralick features for each genotype in A–D. Error bars represent mean ± SEM. Red dotted lines and squares represent mean ± 95% CI from control. Kruskal–Wallis test, H–J: * $p < 0.05$, ** $p < 0.01$, *** $p < 0.001$, **** $p < 0.0001$, ns not significant. Comparison to control is indicated by blue asterisks; comparisons of individuals to each other are indicated by a line and green asterisks. Scale bar: 10 μm.

Coordinated action of myosin with branched and linear actin is required for proper actomyosin ring assembly

Because both linear and branched actin nucleation factors are needed for cell wound repair, yet some actin organization still exists at the wound edge when either type is removed, we next determined what actin organization, if any, remained when linear and branched actin nucleation were removed simultaneously. We could not recover Dia+DAAM+Arp3 triple-knockdown embryos. Thus, we removed linear actin through treatment with C3 exoenzyme (Rho inhibitor; affects several linear nucleators including Dia and DAAM; cf. Matusek *et al.*, 2006; Abreu-Blanco *et al.*, 2014) in an Arp3 knockdown (no branched actin) background (Figure 8, A–B″). Unsurprisingly, removing linear actin by inhibiting Rho1 activity (C3 exoenzyme) in this context severely disrupted the actin cortex and resulted in very few discernable actin structures and failure to close wounds relative to Arp3 RNAi embryos injected with buffer (Figure 8, A, B″, and E), suggesting that branched and linear actin account for the majority, if not all, of the actin organization at wounds.

We next disrupted myosin activity in Arp3 knockdowns by treatment with the ROK inhibitor Y27632. Strikingly, this resulted in the presence of bundled linear actin filaments in the unwounded cortex (Figure 8C). Unsurprisingly, knockdown of Arp3 with additional

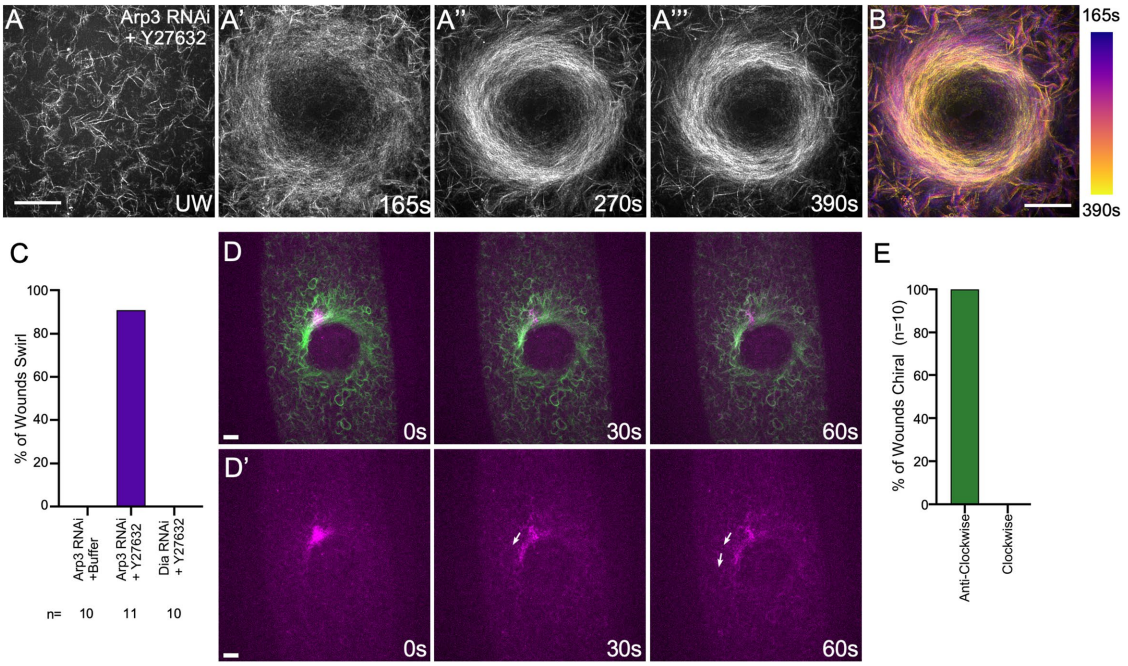

FIGURE 9: In the absence of branched actin and myosin, linear actin filaments swirl to close the wound. (A–A‴) Confocal XY projection images of an Arp3 RNAi embryo treated with Y27632 and expressing the sGMCA actin reporter at unwounded stage, A , 165s, A′, 270 s, A″, and 390 s, A‴. (B) Temporal–color coded projection of actin swirling at the wound depicted in A–A‴ from 165 s (purple) to 390 s (yellow). (C) Quantification of percentage of wounds that exhibited actin filament swirling. (D, D′) Confocal projection images of an Arp3 RNAi embryo expressing a photoconvertible actin reporter (sM3MCA). Photoconverted region showing counterclockwise movement of actin filaments (arrows) is highlighted in D′. (E) Quantification of number of wounds that exhibited actin filament swirling in the counterclockwise direction. Scale bar: 10 μm.

myosin inhibition (Arp3 RNAi + Y27632) resulted in greater fold wound expansion than in control embryos (Arp3 RNAi + Buffer; Figure 8, F and H). In contrast, loss of the majority of branched actin and myosin resulted in greater contraction rates than with Arp3 knockdown alone (Figure 8, F and I). Inhibiting myosin activity also led to a significant reduction ($p < 0.0001$) in the number of actin circles (Figure 8J), suggesting that myosin plays a role in this actin circle formation.

To further examine the bundled actin phenotype in Arp3 RNAi + Y27632, we disrupted myosin in the Dia+DAAM double-knockdown background. The inhibition of linear actin and myosin (Dia+DAAM RNAi + Y27632) led to an unwounded actin cortex consisting primarily of unbundled actin patches (Figure 8, D and D″). This is consistent with branched actin serving as a scaffold for linear actin organization, whereas myosin is needed for branched actin disassembly to prevent its aggregation. Although knockdown of Dia+DAAM did not exhibit significant changes to the initial fold wound expansion or contraction rate, knockdown of Dia+DAAM with myosin inhibition (Dia+DAAM RNAi + Y27632) resulted in severe reduction in wound contraction rates (Figure 8, G–I). In addition, without linear actin or myosin, the number of actin circles is significantly reduced compared with that in controls (Arp3 RNAi + buffer; Figure 8J).

To quantify the actin architectures in these contexts, we performed texture analysis of the wound edge at 70% closure (Figure 8, A′–D′). Embryos treated with Y27632 or C3 exhibited significant ($p < 0.0001$) changes in all four Haralick features from embryos treated with buffer (Figure 8K; Supplemental Table S3), indicating the presence of significantly different actin architectures and/or organization in these different knockdown contexts (Figure 8K).

New mechanism of wound closure in the absence of branched actin and myosin

Without branched actin to serve as a scaffold for building/tethering the actomyosin contractile apparatus, Arp3 knockdowns treated with Y27632 form bundled linear actin filaments in the unwounded cortex (Figure 9A; Video 6). Upon wounding, these bundled linear actin filaments organize and align into striking parallel arrays around the wound edge, which then move in a coordinated manner to reduce the wound area (actin swirling: 91%, $n = 11$; Figure 9, A and B). This movement of actin filaments is not observed in either Arp3 knockdown with buffer injection or Dia knockdown with Y27632 injection (Figure 9C). To identify whether the parallel actin filaments at the wound edge moved together or were sliding past one another in opposite directions, we expressed a photoconvertible actin marker (sM3MCA) to track actin filament movement. Intriguingly, the photoconverted actin reporter on the parallel linear actin filaments consistently moved in a counterclockwise direction (100%, $n = 10$; Figure 9, D and E), suggesting specific chirality for this newly uncovered wound closure mechanism.

DISCUSSION

Cell wound repair studies in a variety of organisms and systems have revealed that while there is a generally conserved framework for wound closure, several different molecular mechanisms dependent on wound type, size, and/or species can be used to achieve this repair. The *Drosophila* model relies heavily on the formation, and then the dynamic translocation, of a contractile actomyosin ring at the wound periphery. To accomplish this, specific organizations of actin filaments (mixed orientation), nonmuscle myosin, scaffolding proteins, and associated cross-linking proteins must be assembled

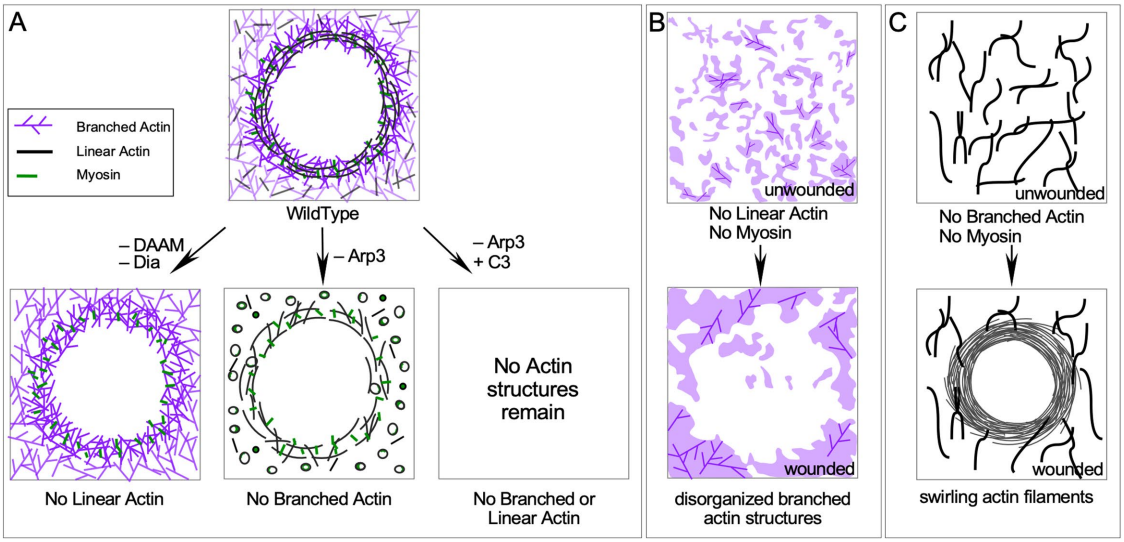

FIGURE 10: Models of branched and linear actin filament coordination during cell wound repair. (A) Branched actin acts as a structural scaffold to hold the linear actin cable at the wound edge. Without branched actin, subunits of the actin cable release from the wound edge and form actin circles due to myosin contraction and bending. Branched and linear actin are vital for cell wound repair, as no actin structures are formed upon Arp3 knockdowns treated with C3 injection. (B) The actin cortex forms large amorphous actin patches in the absence of linear actin and myosin (Dia RNAi + Y27632 treatment). (C) The cell forms large linear actin filaments and bundles in the absence of branched actin and myosin (Arp3 RNAi + Y27632 treatment). Intriguingly, upon wounding, these large linear actin structures are organized at the wound edge and undergo a chiral swirling movement to close the wound.

precisely and then undergo intricately coordinated changes as the actomyosin ring pulls the wound closed. Here we show that ideal cell wound repair requires coordination of linear and branched actin nucleators for the proper assembly and function of the actomyosin ring. We find that the linear actin nucleation factors Dia and DAAM, as well as the WAS family branched actin nucleation–promoting factors WASp and SCAR, exhibit different spatiotemporal recruitment patterns to wounds and have both overlapping and nonredundant roles in the repair process. Interestingly, we find that DAAM, WASp, and to a lesser extent SCAR contribute to actin filament orientation within the actomyosin ring and the loss of branched actin via Arp3 knockdown results in the formation of numerous small actin circles in the cell cortex. Intriguingly, we find that the simultaneous lack of branched actin and myosin activity results in an unexpected actin organization in which an array of parallel actin filament bundles undergoes concerted movement, resulting in a chiral swirling inward to close the wound, uncovering a new mechanism for cell wound closure.

Branched and linear actin coordinate proper actin architecture for cell wound repair

Many diverse cell processes such as cell division, motility, and shape changes require actin filaments to be organized into assemblies of optimized architecture, dynamics, and mechanical attributes to carry out their specific functions properly (Campellone and Welch, 2010; Cheffings *et al.*, 2016; Schwayer *et al.*, 2016; Boiero Sanders *et al.*, 2020; Gautreau *et al.*, 2021). We find that the proper assembly and function of the actomyosin ring require both branched and linear actin networks for proper cell wound repair in the *Drosophila* model (Figure 10A). This is consistent with observations that in vitro actomyosin rings consisting of only linear or only branched actin exhibit impaired contraction (Ennomani *et al.*, 2016). Overlapping bundles of linear actin filaments in mixed orientation, along with nonmuscle myosin motors and cross-linking proteins, make up the contractile actin cable that surrounds the wound periphery (Blanchoin *et al.*, 2014; Cheffings *et al.*, 2016; Schwayer *et al.*, 2016; Muresan *et al.*, 2022). We find that branched actin networks contribute in several ways during cell wound repair: as a scaffold, to influence filament orientation and length, as a foundation to assemble and tether the actomyosin ring, and to aid in anchoring the cortical cytoskeleton to overlying plasma membrane. When branched actin is removed, linear actin bundles are unable to assemble into a functional cable, leading to the formation of long linear actin filament bundles in the wound center. This is consistent with recent findings that the Arp2/3 complex is needed to prevent excessive formin-mediated actin nucleation (Chan *et al.*, 2019). Conversely, we find that a cytoskeleton consisting primarily of branched actin without myosin results in the formation of dispersed amorphous actin structures (Figure 10B). These structures are likely small aggregates of branched networks and are reminiscent of isotropic branched actin networks that are assembled in response to mutant Arp2/3 complexes, but are unproductive since they cannot organize into force-producing actin networks (Narvaez-Ortiz and Nolen, 2022).

Dia and DAAM can both nucleate linear actin filaments, which would be needed to form the actomyosin cable and to serve as the mother filaments for nucleation of branched actin. As knockdown of DAAM, but not Dia, leads to a significant shift in actin filament orientation, DAAM may be associating with myosin to form the actomyosin cable encircling the wound. Dia could then be making the linear actin filaments used by the WAS proteins to generate a branched actin scaffold circumscribing the wound and/or aiding in the tethering of the actomyosin cable to the branched actin scaffold at the wound periphery. This is consistent with Dia being recruited to the wound faster than DAAM or WAS proteins and preceding the formation of the actomyosin ring, as well as the reduced DAAM recruitment to wounds observed in the Arp3 knockdown background.

While WAS family members, along with Arp2/3, promote the generation of branched actin networks, specific family members can be called upon to perform specialized functions within the cell (Burianek and Soderling, 2013; Massaad *et al.*, 2013). These nonredundant functions are often associated with the variable N-terminal domains of WAS family proteins that mediate different protein interactions leading to variations in the architecture of their actin assemblies (Molinie and Gautreau, 2018; Gautreau *et al.*, 2021). Interestingly, all WAS family proteins are needed for proper cell wound repair, but they exhibit different temporal recruitments and repair phenotypes.

Knockdown of WASp leads to a significant shift in actin filament orientation, highlighting the role of branched actin in bending and/or aligning linear actin filaments around the wound edge. Actin filament orientation is important for function, as myosin sliding along linear actin bundles for effective contraction requires a ring geometry with mixed actin filament orientations (Blanchoin *et al.*, 2014; Cheffings *et al.*, 2016). Our findings are also consistent with studies demonstrating a role for WASP in forming actin structures orthogonal to the cell's plasma membrane (Gaertner *et al.*, 2022), as well as polarity during hemocyte (Stramer *et al.*, 2005) and neutrophil (Brunetti *et al.*, 2022) migration.

SCAR knockdown exhibited a wound overexpansion phenotype. We showed previously that E-cadherin functions in cell wound repair to anchor the actomyosin ring to the overlying plasma membrane in cell wound repair (Abreu-Blanco *et al.*, 2011a). Interestingly, a recent report linked the WAVE/SCAR complex and associated branched actin to E-cadherin localization (Sasidharan *et al.*, 2018; Cordova-Burgos *et al.*, 2021) and lamellipodial actin extension (Tang *et al.*, 2020). Therefore, it is possible that *Drosophila* SCAR can play a role in plasma membrane–cytoskeleton anchoring and regulating the overall length of actin filaments in the actin ring. Thus, a complex and dynamic interplay of linear and branched actin is necessary for robust cell wound repair.

Actin circle formation in the absence of branched actin scaffolding

In addition to affecting the actin architecture within the actomyosin ring during cell wound repair, knockdown of Arp3 resulted in the formation of new myosin-associated circular actin structures throughout the cortex. As the actomyosin ring does not form in the absence of anchoring to a branched actin scaffold, one possibility is that these actin/myosin circles are subunits of the actomyosin ring that are unable to assemble into the higher order structure. In this case, linear actin filaments may bend as a result of their association with actin binding proteins (McCullough *et al.*, 2008; Fassler *et al.*, 2020; Harris *et al.*, 2020; Palani *et al.*, 2021). It is also possible that without branched actin, linear filaments bend or encircle themselves due to myosin contraction. Consistent with this, myosin colocalizes with the actin circles, its inhibition abolishes actin circles, and we observe linear actin filaments bending into circles. We find that these actin circles are not observed in the cortex of WT embryos, suggesting that branched actin is presumably inhibiting the formation of this type of architecture. Thus, in the absence of branched actin, the delicate balance of actin binding proteins and branched and linear actin filaments results in the observed actin circles. Further investigations will be needed to elucidate molecular mechanisms behind the formation of actin circles and their functions in the cytoskeleton.

A cell cortex comprised of linear actin filaments only exhibits a new mechanism of wound repair

The molecular mechanisms underpinning actin ring translocation during wound closure can be different depending on the context. *Xenopus* oocytes, for example, can use actin treadmilling to continuously assemble actin at the inner edge of the actin ring and disassemble actin at the outer edge to reduce the wound area (Burkel *et al.*, 2012). *Drosophila* embryos require myosin to form a contractile actomyosin ring assembly to pull the wound closed (Abreu-Blanco *et al.*, 2014). Surprisingly, we observe an unexpected wound repair mechanism when only linear actin filaments are available. In the absence of myosin and branched actin, the remaining linear actin filaments form a parallel array that undergoes a chiral swirling movement wherein actin filaments move directionally to spiral inward and close the wound (Figure 10C). This counterclockwise actin filament swirling in cell wound repair is superficially similar to chiral cytoskeleton assemblies observed in other systems. Active chiral torques are generated to break left/right symmetry in the actomyosin cortex of *C. elegans* embryos and during actin cytoskeleton self-organization in cells with isotropic circular shape (Naganathan *et al.*, 2014; Tee *et al.*, 2015), as well as through the organization of formin-dependent linear actin filaments at immunological synapses (Murugesan *et al.*, 2016). However, in all of these cases, the formation of the chiral cytoskeleton torques depend on myosin activity, whereas the chiral actin filament swirling during cell wound repair occurs in its absence. One class of proteins that has been shown to enhance the contractility of myosin-independent (as well as myosin-dependent) actin rings in vitro is actin cross-linkers (Ennomani *et al.*, 2016; Kucera *et al.*, 2021). Loss of myosin and branched actin leads to a sparse actin network that consists mainly of larger bundles of actin, thus making actin cross-linkers a strong candidate to drive this phenotype. Future investigations will be needed to elucidate the precise molecular mechanism leading to this chiral swirling phenotype.

Thus, while cells prefer to use highly orchestrated interactions among branched actin, linear actin, and myosin to efficiently close wounds, they can nevertheless coopt whatever actin structures are available—branched actin only, linear actin plus myosin, or linear actin only—to close wounds (albeit more slowly). Future investigations will continue to unravel the complexities of these dynamic actin structures and identify the possible molecular triggers that dictate actin ring contraction, treadmilling, and/or filament swirling, as well as the roles of accessory actin binding proteins (i.e., cross-linkers) that can influence their spatiotemporal localizations, thus affecting the actin architecture and the overall mechanics of the cytoskeleton.

MATERIALS AND METHODS

Request a protocol through *Bio-protocol*.

Fly stocks and genetics

Flies were cultured and crossed at 25°C on yeast–cornmeal–molasses–malt extract medium. Flies used in this study are listed in Supplemental Table S1. RNAi lines were driven using the maternally expressed GAL4-UAS driver Pmatalpha-GAL-VP16V37.

An actin reporter, sGMCA (spaghetti squash driven, moesin-alpha-helical-coiled and actin binding site fused to GFP) reporter (Kiehart *et al.*, 2000) or the mScarlet-i fluorescent equivalent, sStMCA (Nakamura *et al.*, 2020), was used to follow the wound repair dynamics of the cortical cytoskeleton.

In this study, we used an actin reporter + maternal GAL4 driver + *vermilion* RNAi (unrelated fly RNAi) as the control. For DAAM RNAi2, we used a DAAM-GFP knock-in (Molnar *et al.*, 2014) with the iGFPi technique (Pastor-Pareja and Xu, 2011). EGFP-shRNA was expressed by the maternal GAL4 driver in a DAAM-GFP background and actin was visualized by sStMCA.

Localization patterns and mutant analyses were performed at least twice with independent genetic crosses and at least 10 embryos were examined. Images representing the average phenotype were selected for figures.

GFP-tagged Scar reporter

To generate GFP-SCAR under its endogenous promoter, we first amplified full-length Scar including the 5′-UTR and the 3′-UTR and cloned it into pBluescript using 5′KpnI and 3′SalI restriction sites. We then fused the 5′-UTR, GFP, and Scar up to the internal XbaI site. This fragment was then fused from the *Xba*I internal site to the end of the 3′-UTR and cloned into pCasper using 5′*Kpn*I and 3′*Not*I restriction sites.

mScarlet-tagged Dia reporter

To generate 3xUASz-StFP-Dia, we first replaced the 10xUAS and syn21 sequence in the 10xUASz-p10 construct (DeLuca and Spradling, 2018) with only 3xUAS. We then cloned the 3xUASz-p10 construct into pCasper. We next amplified full-length Dia ORF and fused it to the 3′ end of mScarlet-i. The resulting StFP-Dia construct was cloned into the 3xUASz-p10 vector using 5′*Kpn*I and 3′*Xba*I restriction sites.

Scarlet-tagged spaghetti squash knock-in (sqh-StFP)

sqh-StFP was generated using CRISPR-mediated homologous recombination. gRNA (5′-TTACTGCTCATCCTTGTCCT-3′) was cloned into pCFD5 vector (Port *et al.*, 2014; Addgene #73914) and then the resulting vector was injected into the attP2 site (BDSC #25710). Subsequently, third chromosome insertion transgenic pCFD5-sqh flies were crossed into w^- backgrounds. To generate the donor vector, mScarlet-i and 2kb homology arms were amplified; then all three fragments were fused and cloned into the pBluescriptII KS(+) vector so that mScarlet-i was inserted just before the stop codon of the *sqh* gene. The donor vector was injected into embryos resulting from crossing nos-Cas9 (BDSC #78782 that had been crossed into a *w*- background) and pCFD5-sqh flies. The mScarlet-i insertion was confirmed by sequencing and the sqh-StFP knock-in flies were viable and fertile.

Photoconvertible actin reporter (sM3MCA)

To generate sM3MCA (spaghetti squash–driven, mScarlet fluorescent protein, moesin-α-helical-coiled and actin binding site), we replaced the mCherry sequence in sChMCA with mMaple3 (Wang *et al.*, 2014) using standard PCR and cloning techniques.

Embryo handling and preparation

Nuclear cycle 4–6 embryos were collected for 30 min at 25°C and harvested at room temperature (22°C). Collected embryos were dechroionated by hand, mounted onto No. 1.5 coverslips coated with glue, and covered with Series 700 halocarbon oil (Halocarbon Products Corp.) as previously described (Abreu-Blanco *et al.*, 2011a).

Drug injections

Pharmacological inhibitors were injected into NC4–6 staged *Drosophila* embryos, incubated at room temperature (22°C) for 5 min, and then subjected to laser wounding. The following inhibitors were used: C3 exoenzyme (1 mg/ml; Cytoskeleton, Inc), NSC23766 (50 mM; Tocris Bioscience), and Y27632 (60 mM; Tocris Bioscience). The inhibitors were prepared in injection buffer (5 mM KCl, 0.1 mM NaP, pH 6.8). Injection buffer alone was used as the control. To label plasma membrane, FM4-64 dye (5 mM; Invitrogen) was injected into the perivitelline space surrounding the embryo.

Laser wounding

All wounds were generated using a pulsed nitrogen N2 micropoint laster (Andor Technology) set to 435 nm and focused on the lateral surface of the embyro. A 16 × 16–μm circular region was set as the target site along the lateral midsection of the embryo, and ablation was controlled by MetaMorph software (Molecular Devices). Average ablation time was less than 3 s and time-lapse image acquisition was initiated immediately after ablation.

Live image acquisition

All live imaging was performed at room temperature with the following microscopes:

1) Revolution WD systems (Andor Technology) were mounted on a Leica DMi8 (Leica Microsystems) with a 63×/1.4 NA objective lens under the control of MetaMorph software (Molecular Devices). Images were captured using 488-nm and/or 561-nm lasers with a Yokogawa CSU-W1 confocal spinning disk head attached to an Andor iXon Ultra 897 EMCCD camera (Andor Technology). Time-lapse images were acquired with 17–20-μm stacks/0.25-μm steps. Images were acquired every 30 s for 15 min and then every 60 s for 15 min. To determine the order of actin nucleator recruitment, images were acquired every 10 s for 5 min.
2) An UltraVIEW VoX Confocal Imaging System (Perkin Elmer, Waltham, MA) was mounted on a Nikon Eclipse Ti (Nikon Instruments, Melville, NY) with a 60×/1.4 NA objective lens under the control of Volocity software(v.5.3.0, Perkin–Elmer). Images were captured using 488-nm and/or 561-nm lasers with a Yokogawa CSU-X1 confocal spinning disk head attached to a Hamamatsu C9100-13 EMCCD camera (Perkin–Elmer, Waltham, MA). Time-lapse images were acquired with 17–20-μm stacks/0.25-μm steps. Images were acquired every 30 s for 15 min and then every 60 s for 15 min.
3) A Dragonfly 200 high-speed confocal imaging platform (Andor Technology) was mounted on a Leica DMi8 (Leica Microsystems) with a 100×/1.4 NA objective lens under the control of Fusion version 2.3.0.36 (Oxford Instruments). Images were captured using 488-nm and/or 561-nm lasers with an Andor iXon Life 888 EMCCD camera (Andor Technology) with the 2× mag changer. Time-lapse images were acquired with 10-μm stacks/0.25-μm steps every 1 min for 30 min and deconvolved using ClearView (Oxford Instruments) deconvolution.

Live photoconversion acquisition

Photoconvertion for sM3MCA was performed using a Mosaic (Andor Technology) on a Revolution WD system. Selected regions of interest (ROIs) were activated by a 405-nm laser for 80–90 ms.

Live super resolution image acquisition

Superresolution imaging was performed using a VT-iSIM (VisiTech International) mounted on a Leica DMi8 (Leica Microsystems) with a 100×/1.4 NA objective lens under the control of MetaMorph software (Molecular Devices). Images were acquired using a 488-nm laser using an Orca-Fusion C14440-20UP camera (Hamamatsu Photonics). Time-lapse images were acquired with 10-μm stacks/0.25-μm steps every 15 s for 15 min or 15 s for 7.5 min followed by every 1 min for 2min and deconvolved using the Fiji plug-in Microvolution (Microvolution LLC).

Image processing, analysis, and quantification

Image processing was performed using FIJI software (Schindelin *et al.*, 2012). In all images, the top side is the anterior and the

bottom side is the posterior of embryos. Kymographs were generated using the crop feature to select ROIs of 5.3 × 94.9 µm. Wound area was manually measured using Fiji and the values were imported into Prism 8.2.1 (GraphPad Software) to construct corresponding graphs.

For fluorescent line plots, the mean fluorescence profile intensities were calculated from 51 equally spaced radial profiles anchored at the center of the wound, swept from 0° to 180°. Radial profiles of diameter 301 pixels were used. For Video 5, a diameter of 600 pixels was used to generate the line plots. Fluorescence intensity profiles were calculated and averaged using an in-house code (available at https://github.com/FredHutch/wound_radial_lineplot) using MATLAB R2020b (MathWorks). For dynamic line plots, we generated fluorescent profile plots from each time point and then concatenated them. The lines represent the averaged fluorescent intensity and the gray area is the 95% confidence interval. Line profiles from the left to the right correspond to the top to bottom of the images unless otherwise noted.

Figures were assembled in Canvas Draw 6 for Mac (Canvas GFX).

Actin circle quantification

Actin circles were counted using 300 × 300–pixel areas (380 µm^2) of the deconvolved single *z*-slice actin cortex. Two nonoverlapping cropped areas were used per embryo.

Texture analysis

Actin architecture was assessed using cropped sections of deconvolved single *z*-slice images 0.25–0.5 µm from the surface of the cortex of the actin ring at 70% wound closure. The gray-level cooccurrence matrix of eight 50 × 50–pixel cropped areas of the wound edge was used to compute four texture-related statistical properties per embryo, variance/contrast (the intensity between a pixel and its neighbor), correlation (linear dependency), uniformity (constancy of intensity level distribution), and homogeneity (the tightness of distribution; Haralick *et al.*, 1973), similar to those previously described (Nakamura *et al.*, 2020). Textural features were extracted using MATLAB R2020b (MathWorks) and were graphed on radar charts and dot plots using R.

Filament orientation

Filament orientation was determined using a method similar to that described previously (Li and Munro, 2021) using Matlab 2020b (MathWorks). First, 400 × 400–pixel deconvolved single *z*-slice images of the actin ring at 70% wound closure were selected to determine the orientation of actin filaments. The images were convolved using the Sobel operator and the gradient intensity and gradient direction from the DV axis were retrieved. The orthogonal direction of the intensity gradient is the filament orientation. To focus on the filaments at the edge of the wound, we limited the analysis to the pixels more than 150 pixels and less than 200 pixels from the center of the wound. Additionally, we placed a threshold based on the magnitude of the intensity gradient to remove background noise. The actin filament distribution was plotted on a radial histogram for visualization. Additionally, the orientation bias was calculated as a ratio of the density of filaments with orientations between 80°–90° and 0°–10°. This was calculated and graphed in R.

Actin–Myosin/Dia/DAAM colocalization

Actin (sGMCA or sStMCA) colocalization with myosin-stFP, GFP-Dia, or DAAM-GFP was calculated in two regions: the center of the wound and the actin ring region (wound periphery). Eight 50 × 50–pixel cropped sections were used per region per embryo to perform the analysis. Pearson's correlation calculations were determined using *cor.test()* in R. Statistical comparisons were conducted by comparing the actin channel with a spatially scrambled version of myosin, Dia, or DAAM in the cropped image.

Quantification of efficiencies in RNAi knockdowns

RNAi knockdown efficiency was quantified using either qPCR or Western blots. To harvest total RNA for qPCR, 100–150 embryos were collected after 30 min incubation at 25°C and treated with TRIzol (Invitrogen/Thermo Fisher Scientific) and then with DNase I (Sigma). Total RNA (1 µg) was reverse transcribed using an iScript gDNA Clear cDNA Synthesis Kit (Bio-Rad). RT-PCR was performed using the iTaq Universal SYBR Green Supermix (Bio-Rad) and primers obtained from the Fly Primer Bank listed in Supplemental Table S1. The percentage knockdown for each gene was derived from two individual parent sets, and each of these biological replicates was run with two technical replicates on the CFX96 Real Time PCR Detection System (Bio-Rad) for a total of four samples per gene. RpL32 (RP-49) was used as reference genes and the knockdown efficiency (%) compared with the control (*vermilion* RNAi only) was obtained using the ΔΔCq calculation method (Supplemental Figure S1I). Dia RNAi knockdown efficiency was previously shown to be 84% via western blot (Abreu-Blanco *et al.*, 2014). Wash RNAi1 and RNAi2 knockdown efficiency were previously identified to be 99% and 96%, respectively, via Western blot (Verboon *et al.*, 2015a,b).

Western blotting

To generate embryo whole-cell lysates, embryos were collected every 30 min and aged to obtain embryos at nuclear cycles 4–6. Embryos were washed in 1X PBS and flash frozen. Embryos were then homogenized in 2× sample buffer (125 mM Tris-Cl pH 6.8, 4% SDS, 0.1% Bromophenol blue, 20% glycerol). Western blotting was performed according to standard procedures using the following antibodies: anti-DAAM (1:1,000; Matusek *et al.*, 2006), anti-Dia (1:5000; Afshar *et al.*, 2000), anti-SCAR P1C1 (1:10; Rodriguez-Mesa *et al.*, 2012), anti-actin (1:1,000; Sigma), anti-α-Tubulin (1:5,000; DHSB), and anti-ATP5A (15H4C4; 1:8000; Abcam). The percentage knockdown for each gene in question is the average of two replicates (Supplemental Figure S1J).

Statistical analysis

All statistical analysis was done using Prism 8.2.1 (GraphPad, San Diego, CA). Statistical significance was calculated using the Kruskal–Wallis test with $p < 0.05$ considered significant. * is $p < 0.05$, ** is $p < 0.01$, *** is $p < 0.001$, **** is $p < 0.0001$, and ns is not significant. Welch's *t* test was used for Supplemental Figure S4 and to compare Pearson correlation coefficients in Figure 7.

ACKNOWLEDGMENTS

We thank Jeffrey Verboon for advice and comments on the manuscript, and Tony Cooke for his microscopy expertise. We thank T. Allen for technical help early in the project, and József Mihály, the Fred Hutch/Leica Center of Excellence, the M. J. Murdoch Charitable Trust, FlyBase, the Bloomington Stock Center, the Harvard Transgenic RNAi Project, and the Vienna *Drosophila* Stock Center for information, microscopes, DNAs, flies, and reagents used in this study. This research was supported by NIH HD095798, NIH GM111635, and the Mark Groudine Chair for Outstanding Achievements in Science and Service (to S.M.P.) and NIH/NCI Cancer Center Support Grant P30 CA015704 (for Cellular Imaging Shared Resource).

REFERENCES

Abreu-Blanco MT, Verboon JM, Parkhurst SM (2011a). Cell wound repair in *Drosophila* occurs through three distinct phases of membrane and cytoskeletal remodeling. J Cell Biol 193, 455–464.

Abreu-Blanco MT, Verboon JM, Parkhurst SM (2011b). Single cell wound repair: dealing with life's little traumas. Bioarchitecture 1, 114–121.

Abreu-Blanco MT, Verboon JM, Parkhurst SM (2014). Coordination of Rho family GTPase activities to orchestrate cytoskeleton responses during cell wound repair. Curr Biol 24, 144–155.

Afshar K, Stuart B, Wasserman SA (2000). Functional analysis of the *Drosophila* diaphanous FH protein in early embryonic development. Development 127, 1887–1897.

Alekhina O, Burstein E, Billadeau DD (2017). Cellular functions of WASP family proteins at a glance. J Cell Sci 130, 2235–2241.

Bement WM, Mandato CA, Kirsch MN (1999). Wound-induced assembly and closure of an actomyosin purse string in *Xenopus* oocytes. Curr Biol 9, 579–587.

Blanchoin L, Boujemaa-Paterski R, Sykes C, Plastino J (2014). Actin dynamics, architecture, and mechanics in cell motility. Physiol Rev 94, 235–263.

Boiero Sanders M, Antkowiak A, Michelot A (2020). Diversity from similarity: cellular strategies for assigning particular identities to actin filaments and networks. Open Biol 10, 200157.

Brand AH, Perrimon N (1993). Targeted gene expression as a means of altering cell fates and generating dominant phenotypes. Development 118, 401–415.

Brunetti RM, Kockelkoren G, Raghavan P, Bell GRR, Britain D, Puri N, Collins SR, Leonetti MD, Stamou D, Weiner OD (2022). WASP integrates substrate topology and cell polarity to guide neutrophil migration. J Cell Biol 221.

Buracco S, Claydon S, Insall R (2019). Control of actin dynamics during cell motility. F1000Res 8.

Buracco S, Singh S, Claydon S, Paschke P, Tweedy L, Whitelaw J, McGarry L, Thomason PA, Insall RH (2022). The Scar/WAVE complex drives normal actin protrusions without the Arp2/3 complex, but proline-rich domains are required. bioRxiv, https://doi.org/10.1101/2022.05.14.491902.

Burianek LE, Soderling SH (2013). Under lock and key: spatiotemporal regulation of WASP family proteins coordinates separate dynamic cellular processes. Semin Cell Dev Biol 24, 258–266.

Burkel BM, Benink HA, Vaughan EM, von Dassow G, Bement WM (2012). A Rho GTPase signal treadmill backs a contractile array. Dev Cell 23, 384–396.

Campellone KG, Welch MD (2010). A nucleator arms race: cellular control of actin assembly. Nat Rev Mol Cell Biol 11, 237–251.

Chan FY, Silva AM, Saramago J, Pereira-Sousa J, Brighton HE, Pereira M, Oegema K, Gassmann R, Carvalho AX (2019). The ARP2/3 complex prevents excessive formin activity during cytokinesis. Mol Biol Cell 30, 96–107.

Cheffings TH, Burroughs NJ, Balasubramanian MK (2016). Actomyosin ring formation and tension generation in Eukaryotic Cytokinesis. Curr Biol 26, R719–R737.

Cooper ST, McNeil PL (2015). Membrane repair: mechanisms and pathophysiology. Physiol Rev 95, 1205–1240.

Cordova-Burgos L, Patel FB, Soto MC (2021). E-Cadherin/HMR-1 membrane enrichment is polarized by WAVE-dependent branched actin. J Dev Biol 9, 19.

Courtemanche N (2018). Mechanisms of formin-mediated actin assembly and dynamics. Biophys Rev 10, 1553–1569.

DeLuca SZ, Spradling AC (2018). Efficient expression of genes in the *Drosophila* germline using a UAS promoter free of interference by Hsp70 piRNAs. Genetics 209, 381–387.

Ennomani H, Letort G, Guerin C, Martiel JL, Cao W, Nedelec F, De La Cruz EM, Thery M, Blanchoin L (2016). Architecture and connectivity govern actin network contractility. Curr Biol 26, 616–626.

Fassler F, Dimchev G, Hodirnau VV, Wan W, Schur FKM (2020). Cryo-electron tomography structure of Arp2/3 complex in cells reveals new insights into the branch junction. Nat Commun 11, 6437.

Gaertner F, Reis-Rodrigues P, de Vries I, Hons M, Aguilera J, Riedl M, Leithner A, Tasciyan S, Kopf A, Merrin J, *et al*. (2022). WASp triggers mechanosensitive actin patches to facilitate immune cell migration in dense tissues. Dev Cell 57, 47–62.e49.

Galan JE, Bliska JB (1996). Cross-talk between bacterial pathogens and their host cells. Annu Rev Cell Dev Biol 12, 221–255.

Gautreau AM, Fregoso FE, Simanov G, Dominguez R (2021). Nucleation, stabilization, and disassembly of branched actin networks. Trends Cell Biol.

Golding AE, Visco I, Bieling P, Bement WM (2019). Extraction of active RhoGTPases by RhoGDI regulates spatiotemporal patterning of RhoGTPases. Elife 8, e50471.

Goley ED, Welch MD (2006). The ARP2/3 complex: an actin nucleator comes of age. Nat Rev Mol Cell Biol 7, 713–726.

Haralick RM, Shanmugam K, Dinstein I (1973). Textural features for image classification. IEEE T Syst Man Cyb Smc3, 610–621.

Harris AR, Jreij P, Belardi B, Joffe AM, Bausch AR, Fletcher DA (2020). Biased localization of actin binding proteins by actin filament conformation. Nat Commun 11, 5973.

Howard AC, McNeil AK, Xiong F, Xiong WC, McNeil PL (2011). A novel cellular defect in diabetes: membrane repair failure. Diabetes 60, 3034–3043.

Hui J, Stjepic V, Nakamura M, Parkhurst SM (2022). Wrangling actin assemblies: actin ring dynamics during cell wound repair. Cells 11, 2777.

Kiehart DP, Galbraith CG, Edwards KA, Rickoll WL, Montague RA (2000). Multiple forces contribute to cell sheet morphogenesis for dorsal closure in *Drosophila*. J Cell Biol 149, 471–490.

Kramer DA, Piper HK, Chen B (2022). WASP family proteins: molecular mechanisms and implications in human disease. Eur J Cell Biol 101, 151244.

Kucera O, Siahaan V, Janda D, Dijkstra SH, Pilatova E, Zatecka E, Diez S, Braun M, Lansky Z (2021). Anillin propels myosin-independent constriction of actin rings. Nat Commun 12, 4595.

Li Y, Munro E (2021). Filament-guided filament assembly provides structural memory of filament alignment during cytokinesis. Dev Cell 56, 2486–2500.e2486.

Massaad MJ, Ramesh N, Geha RS (2013). Wiskott–Aldrich syndrome: a comprehensive review. Ann NY Acad Sci 1285, 26–43.

Matusek T, Djiane A, Jankovics F, Brunner D, Mlodzik M, Mihaly J (2006). The *Drosophila* formin DAAM regulates the tracheal cuticle pattern through organizing the actin cytoskeleton. Development 133, 957–966.

McCullough BR, Blanchoin L, Martiel JL, De la Cruz EM (2008). Cofilin increases the bending flexibility of actin filaments: implications for severing and cell mechanics. J Mol Biol 381, 550–558.

Millard TH, Sharp SJ, Machesky LM (2004). Signalling to actin assembly via the WASP (Wiskott–Aldrich syndrome protein)-family proteins and the Arp2/3 complex. Biochem J 380, 1–17.

Molinie N, Gautreau A (2018). The Arp2/3 regulatory system and its deregulation in cancer. Physiol Rev 98, 215–238.

Molnar I, Migh E, Szikora S, Kalmar T, Vegh AG, Deak F, Barko S, Bugyi B, Orfanos Z, Kovacs J, *et al*. (2014). DAAM is required for thin filament formation and Sarcomerogenesis during muscle development in *Drosophila*. PLos Genet 10, e1004166.

Muresan CG, Sun ZG, Yadav V, Tabatabai AP, Lanier L, Kim JH, Kim T, Murrell MP (2022). F-actin architecture determines constraints on myosin thick filament motion. Nat Commun 13, 7008.

Murugesan S, Hong J, Yi J, Li D, Beach JR, Shao L, Meinhardt J, Madison G, Wu X, Betzig E, Hammer JA (2016). Formin-generated actomyosin arcs propel T cell receptor microcluster movement at the immune synapse. J Cell Biol 215, 383–399.

Naganathan SR, Furthauer S, Nishikawa M, Julicher F, Grill SW (2014). Active torque generation by the actomyosin cell cortex drives left-right symmetry breaking. Elife 3, e04165.

Nakamura M, Dominguez ANM, Decker JR, Hull AJ, Verboon JM, Parkhurst SM (2018). Into the breach: how cells cope with wounds. Open Biol 8.

Nakamura M, Verboon JM, Parkhurst SM (2017). Prepatterning by RhoGEFs governs Rho GTPase spatiotemporal dynamics during wound repair. J Cell Biol 216, 3959–3969.

Nakamura M, Verboon JM, Prentiss CL, Parkhurst SM (2020). The kinesin-like protein Pavarotti functions noncanonically to regulate actin dynamics. J Cell Biol 219, e201912117.

Narvaez-Ortiz HY, Nolen BJ (2022). Unconcerted conformational changes in Arp2/3 complex integrate multiple activating signals to assemble functional actin networks. Curr Biol 32, 975–987.e976.

Palani S, Ghosh S, Ivorra-Molla E, Clarke S, Suchenko A, Balasubramanian MK, Koster DV (2021). Calponin-homology domain mediated bending of membrane-associated actin filaments. Elife 10.

Pastor-Pareja JC, Xu T (2011). Shaping cells and organs in *Drosophila* by opposing roles of fat body-secreted collagen IV and perlecan. Dev Cell 21, 245–256.

Port F, Chen HM, Lee T, Bullock SL (2014). Optimized CRISPR/Cas tools for efficient germline and somatic genome engineering in *Drosophila*. Proc Nat Acad Sci USA 111, E2967–E2976.

Rodriguez-Mesa E, Abreu-Blanco MT, Rosales-Nieves AE, Parkhurst SM (2012). Developmental expression of *Drosophila* Wiskott–Aldrich Syndrome family proteins. Dev Dyn 241, 608–626.

Rorth P (1998). Gal4 in the *Drosophila* female germline. Mech Dev 78, 113–118.

Sasidharan S, Borinskaya S, Patel F, Bernadskaya Y, Mandalapu S, Agapito M, Soto MC (2018). WAVE regulates Cadherin junction assembly and turnover during epithelial polarization. Dev Biol 434, 133–148.
Schindelin J, Arganda-Carreras I, Frise E, Kaynig V, Longair M, Pietzsch T, Preibisch S, Rueden C, Saalfeld S, Schmid B, *et al*. (2012). Fiji: an open-source platform for biological-image analysis. Nat Methods 9, 676–682.
Schwayer C, Sikora M, Slovakova J, Kardos R, Heisenberg CP (2016). Actin rings of power. Dev Cell 37, 493–506.
Sonnemann KJ, Bement WM (2011). Wound repair: toward understanding and integration of single-cell and multicellular wound responses. Annu Rev Cell Dev Biol 27, 237–263.
Stramer B, Wood W, Galko MJ, Redd MJ, Jacinto A, Parkhurst SM, Martin P (2005). Live imaging of wound inflammation in *Drosophila* embryos reveals key roles for small GTPases during in vivo cell migration. J Cell Biol 168, 567–573.
Takenawa T, Suetsugu S (2007). The WASP–WAVE protein network: connecting the membrane to the cytoskeleton. Nat Rev Mol Cell Biol 8, 37–48.
Tang Q, Schaks M, Koundinya N, Yang C, Pollard LW, Svitkina TM, Rottner K, Goode BL (2020). WAVE1 and WAVE2 have distinct and overlapping roles in controlling actin assembly at the leading edge. Mol Biol Cell 31, 2168–2178.
Tee YH, Shemesh T, Thiagarajan V, Hariadi RF, Anderson KL, Page C, Volkmann N, Hanein D, Sivaramakrishnan S, Kozlov MM, Bershadsky AD (2015). Cellular chirality arising from the self-organization of the actin cytoskeleton. Nat Cell Biol 17, 445–457.
Velnar T, Bailey T, Smrkolj V (2009). The wound healing process: An overview of the cellular and molecular mechanisms. J Int Med Res 37, 1528–1542.
Verboon JM, Rahe TK, Rodriguez-Mesa E, Parkhurst SM (2015a). Wash functions downstream of Rho1 GTPase in a subset of *Drosophila* immune cell developmental migrations. Mol Biol Cell 26, 1665–1674.
Verboon JM, Rincon-Arano H, Werwie TR, Delrow JJ, Scalzo D, Nandakumar V, Groudine M, Parkhurst SM (2015b). Wash interacts with lamin and affects global nuclear organization. Curr Biol 25, 804–810.
Wang S, Moffitt JR, Dempsey GT, Xie XS, Zhuang X (2014). Characterization and development of photoactivatable fluorescent proteins for single-molecule-based superresolution imaging. Proc Nat Acad Sci USA 111, 8452–8457.